



**HAL**  
open science

## Latitudinal and Longitudinal Patterns of Exhumation in the Andes of North-Central Chile

María. Pía. Rodríguez, Reynaldo Charrier, Stephanie Brichau, Sébastien Carretier, Marcelo Farías, Philippe de Parseval, Richard A. Ketcham

► **To cite this version:**

María. Pía. Rodríguez, Reynaldo Charrier, Stephanie Brichau, Sébastien Carretier, Marcelo Farías, et al.. Latitudinal and Longitudinal Patterns of Exhumation in the Andes of North-Central Chile. *Tectonics*, 2018, 37, pp.2863-2886. 10.1029/2018TC004997 . insu-03661393

**HAL Id: insu-03661393**

**<https://insu.hal.science/insu-03661393>**

Submitted on 6 May 2022

**HAL** is a multi-disciplinary open access archive for the deposit and dissemination of scientific research documents, whether they are published or not. The documents may come from teaching and research institutions in France or abroad, or from public or private research centers.

L'archive ouverte pluridisciplinaire **HAL**, est destinée au dépôt et à la diffusion de documents scientifiques de niveau recherche, publiés ou non, émanant des établissements d'enseignement et de recherche français ou étrangers, des laboratoires publics ou privés.

Copyright

# Tectonics

## RESEARCH ARTICLE

10.1029/2018TC004997

### Key Points:

- Exhumation next to the western topographic front occurred mostly during the Eocene north of 31.5°S and during the Miocene, south of 31.5°S
- Late Miocene exhumation along the eastern reaches of the studied region is probably the consequence of the onset of flat subduction
- The Paleozoic crystalline core of the Main Cordillera seems to have acted as a buttress for shortening during the Eocene

### Supporting Information:

- Supporting Information S1
- Data Set S1
- Data Set S2
- Data Set S3
- Data Set S4

### Correspondence to:

M. P. Rodríguez,  
 maria.p.rodriguez@gmail.com

### Citation:

Rodríguez, M. P., Charrier, R., Brichau, S., Carretier, S., Fariás, M., de Parseval, P., & Ketcham, R. A. (2018). Latitudinal and longitudinal patterns of exhumation in the Andes of north-central Chile. *Tectonics*, 37, 2863–2886. <https://doi.org/10.1029/2018TC004997>




Received 8 FEB 2018

Accepted 26 JUL 2018

Accepted article online 6 AUG 2018

Published online 6 SEP 2018

## Latitudinal and Longitudinal Patterns of Exhumation in the Andes of North-Central Chile

María Pía Rodríguez<sup>1,2</sup> , Reynaldo Charrier<sup>1,2,3</sup>, Stephanie Brichau<sup>4</sup>, Sébastien Carretier<sup>1,4</sup>, Marcelo Fariás<sup>1</sup> , Philippe de Parseval<sup>4</sup> , and Richard A. Ketcham<sup>5</sup>

<sup>1</sup>Departamento de Geología, Facultad de Ciencias Físicas y Matemáticas, Universidad de Chile, Santiago, Chile, <sup>2</sup>Advance Mining Technology Center, Facultad de Ciencias Físicas y Matemáticas, Universidad de Chile, Santiago, Chile, <sup>3</sup>Escuela de Ciencias de la Tierra, Universidad Andres Bello, Santiago, Chile, <sup>4</sup>Géosciences Environnement Toulouse, Université de Toulouse, UPS, IRD, CNRS, GET, Toulouse, France, <sup>5</sup>Department of Geological Sciences, Jackson School of Geosciences, The University of Texas at Austin, Austin, TX, USA

**Abstract** New thermochronometric data provide evidence for an along-strike diachronous building of the Andes in north-central Chile (28.5–32°S). Geochronological (U-Pb zircon) and thermochronological (apatite fission track and (U-Th)/He) analyses of rock units were obtained in west-to-east transects across the western topographic front. Thermal models indicate that the area west of the topographic front was little exhumed since approximately 45 Ma. To the east of the western topographic front, the Main Cordillera shows both latitudinal and longitudinal differences in exhumation patterns. North of 31.5°S, Cenozoic exhumation began before approximately 40–30 Ma at the western and eastern limits of the Main Cordillera, building the Incaic Range. Later, accelerated exhumation focused on the core of the Main Cordillera and in the Frontal Cordillera at approximately 22–14 Ma and approximately 7 Ma, respectively. South of 31.5°S, accelerated exhumation in the Main Cordillera occurred mainly around 22–14 Ma, after an initial Eocene phase, and the locus of exhumation moved eastward by the late Miocene. Whereas accelerated exhumation in the early to mid-Miocene correlates with the breakup of the Farallon Plate, late Miocene accelerated exhumation correlates with the onset of flat subduction. Latitudinal differences on the exhumation timing along the western topographic front of the Main Cordillera may be due to the absence of the Paleozoic crystalline core south of 31.5°S, which seems to have acted as a buttress for shortening during the Eocene.

### 1. Introduction

The Central Andes (15–34°S; Tassara, 2005) are a type example of an orogen developed in an oceanic-continent subduction context (e.g., Dewey & Bird, 1970). Although modern subduction began in the Early Jurassic, its contractional evolution did not begin before the Late Cretaceous (Charrier et al., 2007). Moreover, most of the tectonic shortening and uplift has been recorded during Cenozoic times (e.g., Charrier et al., 2007; Barnes & Ehlers, 2009). The present-day interaction between the Nazca and South American plates is reflected in the development of a north-to-south oriented highly elevated plateau that reaches its maximum width at the latitude of the Altiplano-Puna, getting systematically narrower and more incised toward the south (Figures 1a and 1b). The plateau is bounded by topographic fronts to the east and west that separate the highest Andes from the adjacent lower elevated areas (Figures 1a and 1b). The eastern topographic front systematically coincides along strike with east vergent active thrust systems that cause intense crustal seismicity along the foreland, (Figure 1a; Alvarado et al., 2005; Alvarado & Ramos, 2011; Costa et al., 2006; Lamb, 2000; Ortiz et al., 2015). In contrast, evidence of active deformation along the western topographic front is scarce and has been recognized only in northern Chile (Figure 1a; west vergent thrust system; Fariás et al., 2005; Garcia & Herail, 2005; Hall et al., 2012; Jordan et al., 2010; Muñoz & Charrier, 1996; Pinto et al., 2007; Victor et al., 2004) and in central Chile (Figure 1a; San Ramón Fault; Armijo et al., 2010; Charrier et al., 2002; Pérez et al., 2013; Rauld, 2011; Vargas et al., 2014). Between 22 and 30°S, structural and thermochronological data suggest that accelerated exhumation along the western topographic front occurred mostly during the Eocene, building the Incaic Range (Figure 1a; Cembrano et al., 2003; Martínez et al., 2017; Lossada et al., 2017; Maksaev & Zentilli, 1999; Sanchez et al., 2017). In contrast, between 33 and 34°S thermochronological data indicate that accelerated exhumation took place from the late Miocene to the Pliocene next to the western topographic front (Maksaev et al., 2009), with ongoing mountain building occurring along the west vergent San Ramón fault (Vargas et al., 2014). The factors controlling the

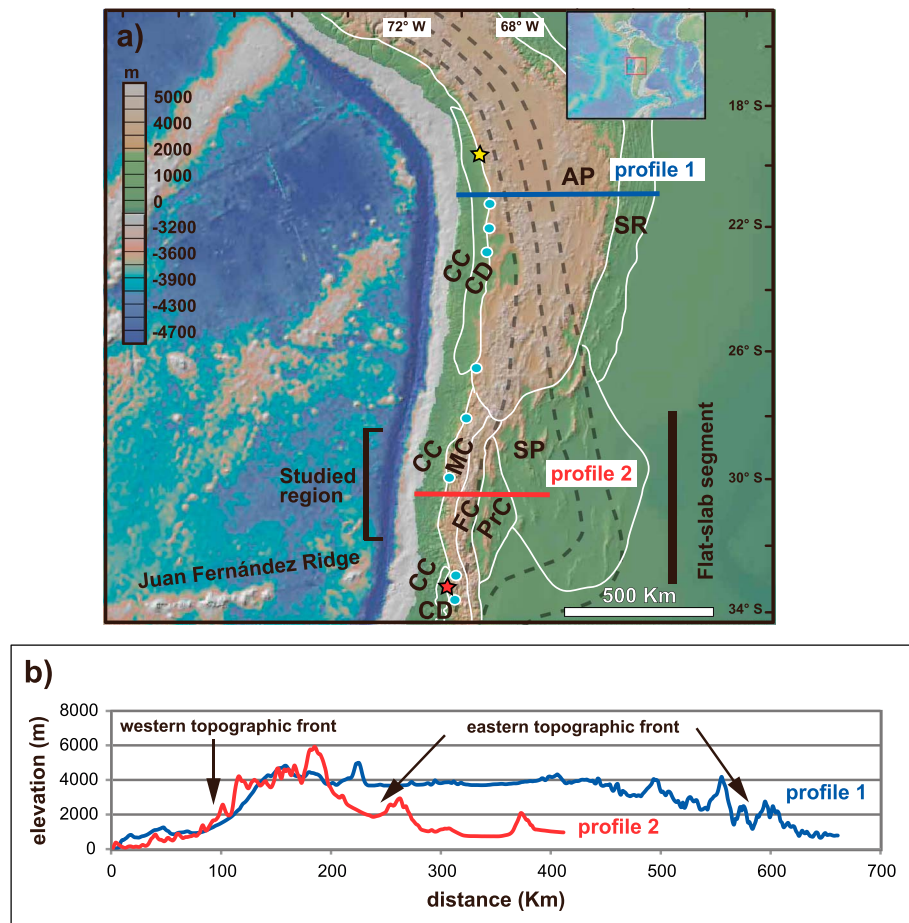


**Figure 1.** (a) Shaded relief image of the Central Andes showing main morphostructural units. The dashed lines mark the isobaths at 50, 100, and 150 km of the Nazca below the South American plate according to Cahill and Isacks (1992). The white lines show the borders between main morphostructural units. CC = Coastal Cordillera, CD = Central Depression, AP = Altiplano-Puna, SR = Subandean Ranges, MC = Main Cordillera, FC = Frontal Cordillera, PrC = Precordillera and SP = Pampean Ranges. The yellow star shows epicenter of crustal earthquakes related to the west-vergent thrust system (WTS) according to Fariás et al. (2005), and the red star shows location of paleoseismological trench of the San Ramón Fault studied by Vargas et al. (2014). Location of thermochronological samples collected next to the western topographic front by Maksiyev and Zentilli (1999), Sanchez et al. (2017), Martínez et al. (2017), Lossada et al. (2017), and Maksiyev et al. (2009) shown by pale blue dots. (b) Topographic profiles across the Altiplano (profile 1) and across the Main and Frontal Cordilleras (profile 2) showing western and eastern topographic fronts.

observed latitudinal differences in exhumation are largely unknown. On one hand, a marked rise in precipitation from 200 mm/year at 33°S to 800 mm/year at 35°S is observed, causing higher fluvial erosion rates southward from 33°S (Fariás, 2007). Thus, it has been suggested that younger thermochronological ages to the south of 33°S would be reflecting such a climatic gradient (Stalder et al., 2017). On the other hand, it has been shown that shallowing of the Nazca slab north of 33°S (Figure 1a) would have shifted the locus of deformation toward the Argentinean foreland since the late Miocene (Ramos et al., 2002; Martinod et al., 2010). Thus, late Miocene to Pliocene thermochronological ages like the ones observed south of 33°S would not be expected along the western topographic front north of 33°S.

Here we present the geochronology and low-temperature thermochronology of north-central Chile (28.5–32°S), which records this transition in exhumation patterns in the development of the Chilean Andes (Figure 1a). In order to recognize variability in exhumation, we applied U-Pb zircon geochronology combined with low-temperature thermochronology, including apatite fission track (AFT) and apatite (U-Th)/He (AHe) on both sides of the western topographic front in this region. We address the following questions: When did the western topographic front develop in this region? Are there any spatial variations on the exhumation

patterns as suggested by thermochronometric data north and south of this region? If so, what are the potential local and regional controls on these variations?

## 2. Regional Setting

The present-day plate tectonic configuration in the Central Andes (15°–34°S) was acquired after the breakup of the Farallon Plate into the Nazca and the Cocos Plates approximately 23 Ma ago (Pardo-Casas & Molnar, 1987; Seton et al., 2012; Somoza, 1998). As a result of this major tectonic plate reorganization, between the late Oligocene and the early Miocene the convergence rate of the Farallon (Nazca) Plate relative to the South American Plate rose from 50 to 60 mm/year to a maximum of 150 mm/year (Pardo-Casas & Molnar, 1987). The current convergence between the Nazca and South American plates is characterized by along-strike variations of the subduction angle from flat  $\sim 10^\circ$  to normal  $\sim 30^\circ$  (Figure 1a; Cahill & Isacks, 1992; Jordan et al., 1983; Pardo et al., 2002). The studied region is located between 28.5 and 32°S, above the Pampean or Chilean flat-slab segment (27–33°S; Figure 1a). Slab flattening has been attributed to the subduction of the buoyant Juan Fernández ridge in the Nazca Plate at the same location in the southern end of the flat slab segment, since approximately 10 Ma (Figure 1a; Yáñez et al., 2001). Contrary to what is observed in the areas north of 27°S and south of 33°S, no Quaternary arc volcanism developed in this region as a result of the reduction in subduction angle and the consequent eastward migration of the asthenospheric wedge. Thus, initiation of slab flattening is mostly inferred from the evolution of arc magmatism, in particular, from the end of andesitic magmatic activity in the main arc of this region approximately 9 Ma (Bissig et al., 2011; Kay & Mpodozis, 2002; Litvak et al., 2007).

The Andean orogen above the flat-slab region consists from west to east of: the north-south oriented Coastal Cordillera, the Main Cordillera, the Frontal Cordillera, the Precordillera, and the Sierras Pampeanas (Figure 1a). The studied region includes the Coastal, Main, and Frontal Cordilleras between 28.5° and 32°S (Figures 1a and 1b and 2). In this area, the Coastal Cordillera is separated from the Main Cordillera by the western topographic front (Figures 1a and 1b), and the traces of the San Félix, Vicuña, and Llimpo faults are roughly aligned along this topographic feature from north to south (Figure 2).

The Coastal Cordillera exposes Paleozoic (Devonian to Carboniferous) metamorphic and metasedimentary basement along the coast, which is unconformably overlain by an east dipping homoclinal succession of Mesozoic (middle Triassic to Upper Cretaceous) volcano-sedimentary units (Figure 2). Both the Paleozoic basement and the Mesozoic volcano-sedimentary rocks are intruded by north-south oriented Mesozoic plutonic belts with decreasing ages to the east: a mid-Triassic to Jurassic belt, an Lower to middle Cretaceous belt, and an Upper Cretaceous to Paleocene belt (Figures 2 and 3). Along the coast and in the bottom of the main valleys the Paleozoic and Mesozoic rocks are unconformably covered by interfingered subhorizontal Cenozoic (lower Miocene to Pleistocene) marine to fluvial continental deposits (Figure 2; Arévalo et al., 2009; Empanan & Pineda, 2006; Pineda & Calderón, 2008; Rivano & Sepúlveda, 1991).

The geology of the Main Cordillera presents a marked change around  $\sim 31.5^\circ$ S. North of  $31.5^\circ$ S it is composed of a core of Paleozoic intrusive (mainly Carboniferous to Permian and minor Permo-Triassic) and minor metamorphic units (Ordovician) flanked to the west by a folded stratified succession of Mesozoic (Triassic to Upper Cretaceous) volcano-sedimentary rocks intruded by a Mesozoic (Upper Cretaceous to Paleocene) belt of plutonic units (Figure 2; Mpodozis & Cornejo, 1988; Nasi et al., 1990; Pineda & Calderón, 2008; Bissig et al., 2011; Martínez et al., 2012, 2016). In this area the eastern border of the Main Cordillera is marked by the east-vergent La Plata reverse fault (Moscoso & Mpodozis, 1988; Mpodozis & Cornejo, 1988; Nasi et al., 1990). Conversely, south of  $31.5^\circ$ S the core of the Main Cordillera consists of Cenozoic (upper Oligocene and Miocene) volcano-sedimentary rocks (Jara & Charrier, 2014; Mpodozis et al., 2009) flanked to the west by Mesozoic (Lower to Upper Cretaceous) sedimentary successions (Figure 2). Upper Cretaceous to Paleocene, Eocene, Oligocene, and Miocene plutonic belts with ages decreasing to the east intrude the Mesozoic and Cenozoic deposits (Figure 2).

In Chile and Argentina the Frontal Cordillera consists of uplifted blocks of mostly Paleozoic to Mesozoic (Permo-Triassic) volcanic and intrusive rocks. To the west, near its border with the Main Cordillera, these blocks are overlain by deformed Mesozoic (Triassic to Upper Cretaceous) volcano-sedimentary rocks, whereas to the east they are covered by Cenozoic (upper Oligocene to Miocene) volcano-sedimentary deposits (Figure 2).

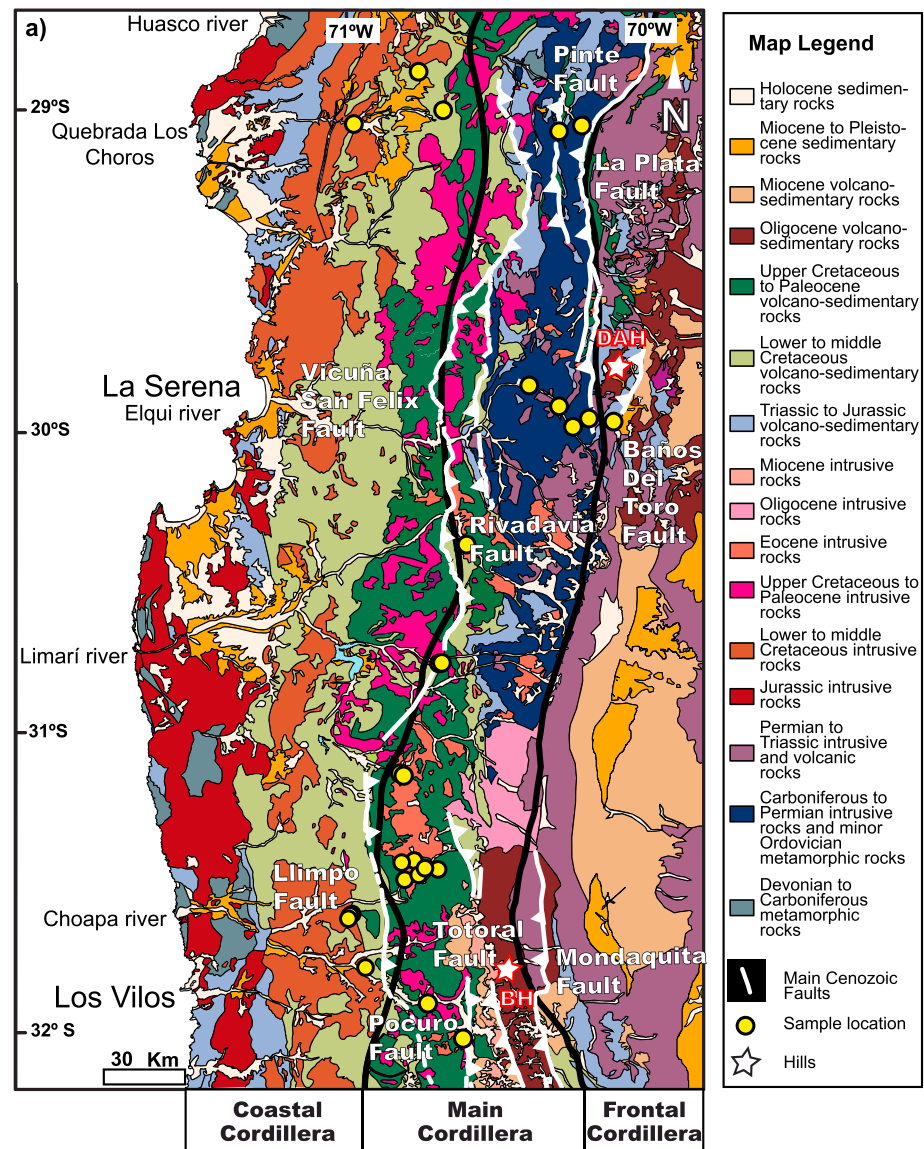


**Figure 2.** (a) Geological map of north-central Chile. Modified from Sernageomin (2003). DHA = Doña Ana Hill, BH = Blanco Hill.

Since the Late Cretaceous the geological evolution in north-central Chile has been characterized by the occurrence of major compressive events followed by periods of apparently milder, though uninterrupted compression (Barnes & Ehlers, 2009; Charrier et al., 2012). However, in Jurassic and Early Cretaceous times, a tensile stress regime caused generalized extension in the continental margin and the development of wide backarc extensional basins (e.g., Charrier et al., 2007), to the east of the magmatic arc. According to the outcrop distribution of Jurassic to Lower Cretaceous volcano-sedimentary and sedimentary rocks (Figure 2), these extensional basins developed mainly along the border between the present-day Coastal and Main Cordilleras and the border between the present-day Main and Frontal Cordilleras (Figure 2). Tectonic inversion of the extensional basins occurred during the Peruvian (late Early to early Late Cretaceous) and the subsequent “K-T” (Cretaceous- Paleogene boundary) and Incaic (mid-late Eocene) orogenic phases (e.g., Amilibia et al., 2008). In the studied region, the west vergent Vicuña-San Félix and the east vergent Rivadavia reverse faults have been joined at depth and interpreted as uplifting the western border of the Main Cordillera northward from 30°S during the Incaic orogeny (Cembrano et al., 2003; Pineda & Emparán, 2006; Pineda & Calderón, 2008), building the Incaic Range (Charrier et al., 2007; Charrier et al., 2009). According to

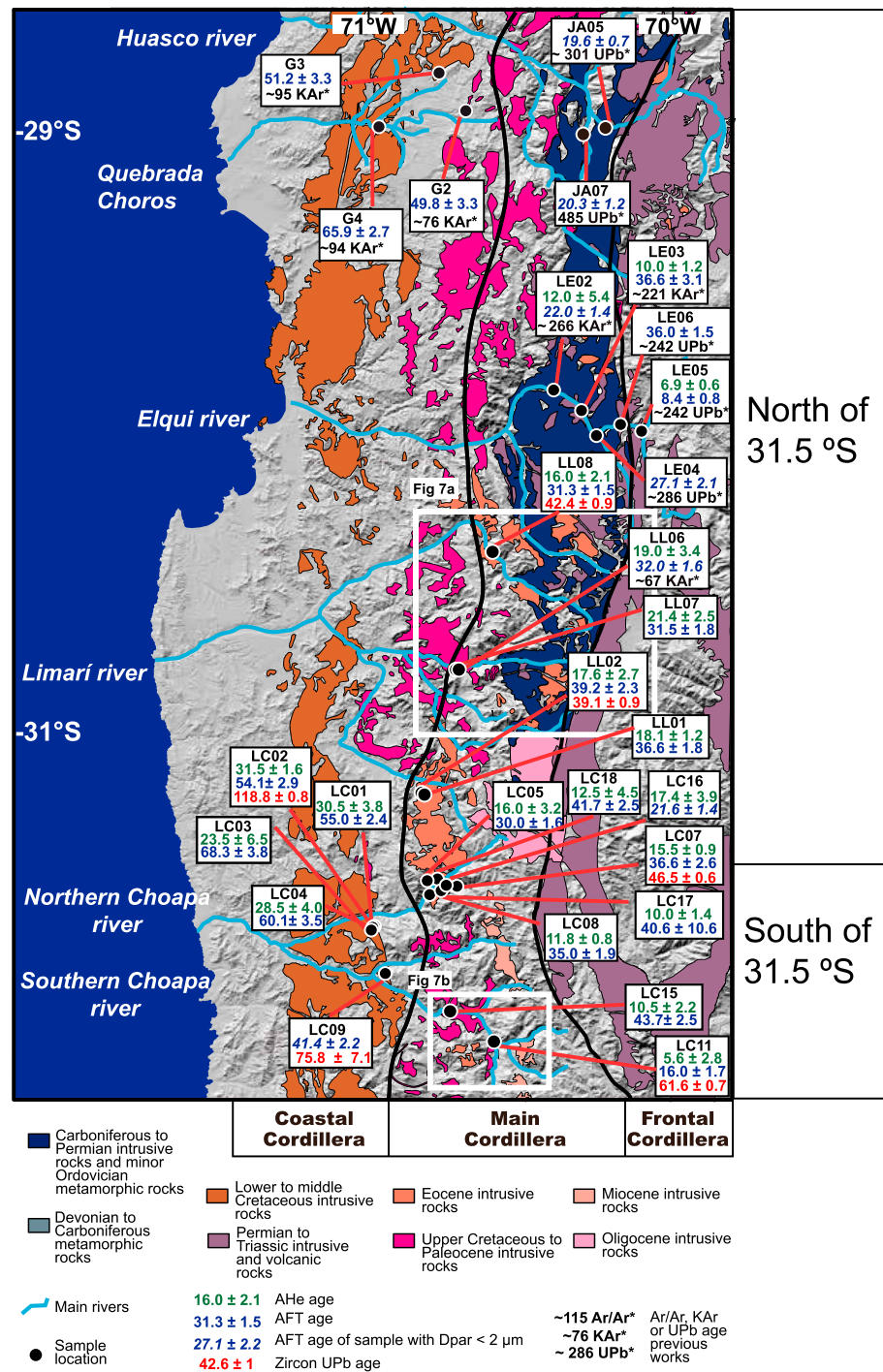


**Figure 3.** U-Pb zircon (red) and AFT (blue, blue italic = samples with  $D_{\text{par}} < 2 \mu\text{m}$ ) and AHe (green) ages in Ma of samples collected throughout north-central Chile. U-Pb errors at  $\pm 2\sigma$ , AFT and AHe errors at  $\pm 1\sigma$ . The solid black lines mark the border between main morphostructural units and subunits. The pale blue lines mark trace of major rivers. Rock ages from previous works (Álvarez et al., 2011; Arévalo et al., 2009; Martin et al., 1999; Nasi et al., 1990; Pankhurst et al., 1996; Pineda & Calderón, 2008) in black and marked with an asterisk, data sources for can be found in the Table 1.

thermochronometric, structural, and paleoelevation data the Incaic Range was a NNE-SSW mountain belt forming the main palaeogeographic feature in southern Peru and northern Chile from the Oligocene to the early Miocene (Armijo et al., 2015; Bissig & Riquelme, 2010; Charrier et al., 2007; Maksiav & Zentilli, 1999). However, the areal extent of this relief into north-central Chile is unclear as no geological records of

mid-late Eocene shortening are known southward from 30°S. Following mid-late Eocene compression, a late Oligocene extensional intra-arc basin developed farther east (Jara & Charrier, 2014; Winocur et al., 2015), along the present-day Frontal Cordillera at 30°S (e.g., outcrops next to Doña Ana Hill in Figure 2), and along the Main Cordillera southwards from 31.5°S (e.g., outcrops next to Blanco Hill in Figure 2). At 30°S the intra-arc basin was successively inverted throughout the Miocene (Winocur, 2010), whereas south of 31.5°S it was inverted during the early Miocene (Charrier et al., 2002; Jara & Charrier, 2014).

East and west vergent high-angle reverse faults cutting through the Main and Frontal Cordilleras are interpreted to have played an important role in Cenozoic uplift (Aguilar et al., 2013; Bissig et al., 2011; Jara & Charrier, 2014; Moscoso & Mpodozis, 1988; Nasi et al., 1990; Mpodozis et al., 2009). North of 31.5°S, some of these faults are the Vicuña-San Félix and Rivadavia Faults, the Pinte and La Plata Faults within the Main Cordillera, and the Baños del Toro Fault within the Frontal Cordillera (Figure 2). South of 31.5°S, the main faults active during the Cenozoic are the Llimpo Fault and the Pocuro, Totoral, and Mondaquita Faults from west to east within the Main Cordillera (Figure 2).

### 3. Sampling Strategy

We collected a total of 28 samples across the Coastal, Main, and Frontal Cordilleras. Analyzed samples are dominantly granitoids, with the exception of JA05 and JA07, which are gneiss (Table 1). Samples were collected in two segments, one to the north of 31.5°S and another one south of 31.5°S (Figures 2 and 3). The objective of our sampling strategy was to identify differences in exhumation timing along the Main Cordillera between the two segments, considering that north of 31.5°S much older rocks are exposed (the Paleozoic crystalline core) than farther south (Figures 2 and 3).

The segment north of 31.5°S includes samples collected from the Coastal, Main, and Frontal Cordilleras and across the topographic front along the Huasco-Quebrada Los Choros, Elqui, and the Limarí valleys. All samples from this segment were collected at the bottom or near the bottom (<500 m) of the valleys (Figure 3). Samples from the Main Cordillera in this segment come from three different domains: one group was collected in the Upper Cretaceous to Paleocene and Eocene intrusive belts next to the western topographic front (LL08, LL06, LL07, LL01, and LL02), the second group was collected from the crystalline Paleozoic core of the Main Cordillera (JA05, JA07 and LE02), and the third was collected close to the eastern border of the Main Cordillera (Figure 4; LE03, LE04, and LE06).

The segment south of 31.5°S includes samples from the Coastal and Main Cordilleras along the northern and southern parts of the Choapa Valley (Figure 3). Along the northern Choapa Valley samples were collected from two vertical profiles, one in the Coastal Cordillera (LC01, LC02, LC03, and LC04), the other one in the Main Cordillera next to the western topographic front (LC05, LC07, LC08, LC16, LC17, and LC18; Figures 3 and 4). Samples LC09 from the Coastal Cordillera and LC15 from the Main Cordillera were collected at the bottom or near the bottom (<500 m) of the valleys in the segment south of 31.5°S (Figure 3).

### 4. Methodology

Low-temperature thermochronology is based on the accumulation of the radioactive decay products of certain isotopes and the temperature-dependent retention of these products. In particular, the AFT (Gallagher et al., 1998; Gleadow et al., 2002) and the (U-Th)/He in apatite (AHe; Flowers et al., 2009; Gautheron et al., 2009) methods are based on the accumulation of tracks caused by fission decay of  $^{238}\text{U}$ , and on the ingrowth of  $^4\text{He}$  produced by U and Th series decay, respectively. Fission tracks in apatite are only partially annealed and shortened in a typical range between ~60 and 120 °C, whereas  $^4\text{He}$  is partially retained in a typical range between ~40 and 80 °C. These closure temperature ranges are generally accurate, but they can change depending on apatite composition in the AFT system (e.g., Green et al., 1986) and on the accumulated radiation damage in the AHe system (e.g., Flowers et al., 2009). The fact that tracks shorten (anneal) in a certain temperature range allows extraction of important information about their cooling paths, as rapidly cooled rocks would display mostly long tracks >14  $\mu\text{m}$ , contrary to slowly cooled rocks that would exhibit shortened tracks <14  $\mu\text{m}$  (Green et al., 1986, Carlson, 1990; Crowley, 1993; Crowley et al., 1991). Importantly, it is widely known that apatites can present different annealing behaviors that are usually linked to compositional variations, with chlorine-rich apatites presenting more resistance to annealing than fluorine-rich apatites (e.g.,

**Table 1**  
U-Pb, AFT, and AHe Data for the Analyzed Samples

Sample	Raw AHe age $\pm 1\sigma$ (Ma)	FTs mean (dmm/s)	AHe age $\pm 1\sigma$ (Ma)	AFT age $\pm 1\sigma$ (Ma)	Mean length $\pm 1\sigma/N^\circ$ tlm ( $\mu\text{m} \pm 1\sigma/N^\circ$ tlm)	Dpar $\pm 1\sigma$ ( $\mu\text{m}$ )	%Cl $\pm 1\sigma$ (%Ox)	Tc range Dpar ( $^\circ\text{C}$ )	Tc range %Cl ( $^\circ\text{C}$ )	U-Pb age $\pm 2\sigma$ or geochronologic ages from other studies (Ma)
North of 31.5°S										
Coastal Cordillera										
G-2	-	-	-	49.8 $\pm$ 3.3	14.21 $\pm$ 1.7/200	2.53 $\pm$ 0.32	-	-	-	76 $\pm$ 2 K-Ar Bt (Arévalo et al., 2009)
G-3	-	-	-	<b>51.2 <math>\pm</math> 3.3</b>	13.57 $\pm$ 2.11/201	2.17 $\pm$ 0.27	-	-	-	95 $\pm$ 2 -Ar Bt (Arévalo et al., 2009)
G-4	-	-	-	65.9 $\pm$ 2.7	14.22 $\pm$ 1.55/204	1.88 $\pm$ 0.14	-	-	-	97 $\pm$ 3 Ma K-Ar Bt (Arévalo et al., 2009)
Main Cordillera										
Next to the topographic front										
LL08	11 $\pm$ 1.8	0.68	16.0 $\pm$ 2.1	31.3 $\pm$ 1.5	15 $\pm$ 1.44/210	2.86 $\pm$ 0.17	1.7 $\pm$ 0.24	122-118	132-125	42.4 $\pm$ 0.9
LL07	16 $\pm$ 2.3	0.74	21.4 $\pm$ 2.5	31.5 $\pm$ 1.8	14.09 $\pm$ 1.53/179	<b>1.75 <math>\pm</math> 0.26</b>	0.25 $\pm$ 0.03	108-101	109-108	~67 K-Ar Bt (Pineda & Calderón, 2008)
LL06	14.2 $\pm$ 2.6	0.74	19.0 $\pm$ 3.4	<b>32.0 <math>\pm</math> 1.6</b>	13.86 $\pm$ 1.3/210	<b>1.73 <math>\pm</math> 0.11</b>	0.33 $\pm$ 0.08	105-102	111-108	
LL01	13.4 $\pm$ 1.1	0.74	18.1 $\pm$ 1.2	<b>36.6 <math>\pm</math> 1.8</b>	14.92 $\pm$ 1.45/210	2.51 $\pm$ 0.18	0.86 $\pm$ 0.17	117-112	119-114	
LL02	12.9 $\pm$ 1.9	0.73	17.6 $\pm$ 2.7	<b>39.2 <math>\pm</math> 2.3</b>	14.69 $\pm$ 1.25/210	2.4 $\pm$ 0.15	0.76 $\pm$ 0.23	116-111	119-112	39.1 $\pm$ 0.9
Axis of basement core										
JA-05	-	-	-	<b>19.6 <math>\pm</math> 0.7</b>	13.79 $\pm$ 1.52/203	<b>1.68 <math>\pm</math> 0.21</b>	-	-	-	~267 Ma U-Pb zr (Alvarez et al., 2011)
JA-07	-	-	-	20.3 $\pm$ 1.2	14.12 $\pm$ 1.38/162	<b>1.61 <math>\pm</math> 0.19</b>	-	-	-	~284 U-Pb zr (Alvarez et al., 2011)
LE02	8.2 $\pm$ 3.9	0.68	12.0 $\pm$ 5.4	<b>22.0 <math>\pm</math> 1.4</b>	14.1 $\pm$ 1.7/132	<b>1.92 <math>\pm</math> 0.13</b>	0.28 $\pm$ 0.05	108-104	109-108	266 $\pm$ 7 Ma K-Ar Amp (Nasi et al., 1990)
Eastern border										
LE06	-	-	-	<b>36.0 <math>\pm</math> 1.5</b>	13.28 $\pm$ 1.84/153	2.12 $\pm$ 0.16	0.03 $\pm$ 0.01	112-107	105-105	~242 Ma U-Pb zr (Martin et al., 1999)
LE04	-	-	-	27.1 $\pm$ 2.1	12.97 $\pm$ 1.86/135	<b>1.63 <math>\pm</math> 0.16</b>	0.04 $\pm$ 0.12	104-101	107-104	~286 Ma U-Pb zr (Pankhuist et al., 1996)
LE03	7.1 $\pm$ 0.9	0.70	10.0 $\pm$ 1.2	36.0 $\pm$ 3.1	13.88 $\pm$ 1.76/210	2.03 $\pm$ 0.16	0.35 $\pm$ 0.15	110-106	112-107	~221 K-Ar Bt (Nasi et al., 1990)
Frontal Cordillera										
LE05	5.1 $\pm$ 0.2	0.74	6.9 $\pm$ 0.6	8.4 $\pm$ 0.8	14.10 $\pm$ 0.13	1.84 $\pm$ 0.4	-	-	-	
South of 31.5°S										
Coastal Cordillera										
vertical section										
LC01	23.9 $\pm$ 2.5	0.78	30.5 $\pm$ 3.8	55.0 $\pm$ 2.4	14.46 $\pm$ 1.53/210	2.01 $\pm$ 0.15	-	-	-	
LC02	25.8 $\pm$ 1.7	0.82	31.5 $\pm$ 1.6	54.1 $\pm$ 2.9	14.68 $\pm$ 1.4/210	2.82 $\pm$ 0.2	2.26 $\pm$ 0.21	122-117	140-133	118.8 $\pm$ 0.8
LC03	17.2 $\pm$ 5.2	0.72	23.5 $\pm$ 6.5	<b>68.3 <math>\pm</math> 3.8</b>	14.55 $\pm$ 1.43/210	2.25 $\pm$ 0.17	-	-	-	
LC04	21.9 $\pm$ 2.9	0.76	28.5 $\pm$ 4.0	60.1 $\pm$ 3.5	14.68 $\pm$ 1.34/156	2.31 $\pm$ 0.28	1.0 $\pm$ 0.26	116-108	122-115	
others										
LC09	-	-	-	41.4 $\pm$ 2.2	13.88 $\pm$ 1.9/184	<b>1.67 <math>\pm</math> 0.11</b>	0.36 $\pm$ 0.15	104-101	112-107	75.8 $\pm$ 7.1
Main Cordillera										
vertical section, next to the topographic front										
LC05	11.2 $\pm$ 2	0.70	16.0 $\pm$ 3.2	<b>30.0 <math>\pm</math> 1.6</b>	14.96 $\pm$ 1.39/210	2.39 $\pm$ 0.19	-	-	-	
LC07	12.2 $\pm$ 0.5	0.78	15.5 $\pm$ 0.9	<b>36.6 <math>\pm</math> 2.6</b>	14.8 $\pm$ 1.49/190	2.4 $\pm$ 0.16	1.12 $\pm$ 1.12	116-111	123-118	46.5 $\pm$ 0.6
LC17	7.1 $\pm$ 0.7	0.71	10.0 $\pm$ 1.4	40.6 $\pm$ 10.6	14.5 $\pm$ 1.9/15	2.32 $\pm$ 0.38	0.89 $\pm$ 0.52	118-107	125-110	
LC16	12.9 $\pm$ 2.2	0.75	17.4 $\pm$ 3.9	21.6 $\pm$ 1.4	14.5 $\pm$ 1.45/90	<b>1.61 <math>\pm</math> 0.14</b>	-	-	-	
LC18	9.1 $\pm$ 3.1	0.73	12.5 $\pm$ 4.5	41.7 $\pm$ 2.5	14.87 $\pm$ 1.51/210	2.59 $\pm$ 0.17	1.44 $\pm$ 0.09	119-113	126-124	
LC08	8.4 $\pm$ 0.9	0.71	11.8 $\pm$ 0.8	35.0 $\pm$ 1.9	14.58 $\pm$ 1.39/210	2.62 $\pm$ 0.18	1.46 $\pm$ 0.09	119-114	126-124	
others										
LC11	4.9 $\pm$ 2.5	0.89	5.6 $\pm$ 2.8	16.0 $\pm$ 1.7	14.57 $\pm$ 1.5/125	2.23 $\pm$ 0.15	0.95 $\pm$ 0.42	113-109	124-112	61.6 $\pm$ 0.7
LC15	7.5 $\pm$ 1.8	0.71	10.5 $\pm$ 2.2	<b>43.7 <math>\pm</math> 2.5</b>	14.59 $\pm$ 2.17/210	2.96 $\pm$ 0.33	0.86 $\pm$ 0.82	126-117	128-105	

Note. Geochronological ages marked with an asterisk were taken from previous works. AFT ages that do not pass the Chi-square test are written in bold italic. AFT samples with Dpar values  $< 2 \mu\text{m}$  are written in bold.



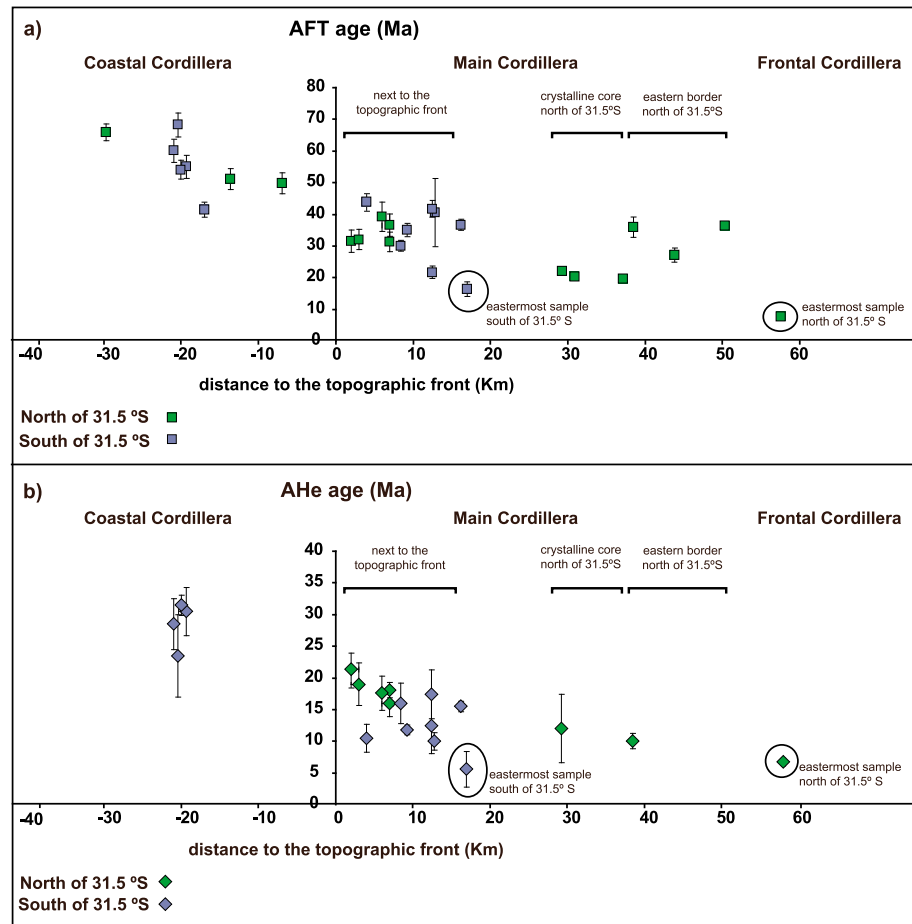


**Figure 4.** (a) AFT ages versus distance to the topographic front. (b) AHe ages versus distance to the topographic front. Errors are  $\pm 1\sigma$  in all figures.

Barbarand et al., 2003; Carlson et al., 1999; Donelick, 1993; Green et al., 1986). Therefore, the temperature at which the AFT age is registered and the temperature range over which tracks anneal depend on the apatite composition. This has important implications in AFT data interpretations when multiple types of apatites are found within a single sample (e.g., Barnes et al., 2006). Variations in apatite annealing behavior can also be inferred by measuring apatite solubility using the diameter of the etch figure (“Dpar”: Donelick, 1993). It is thought that this method can provide prediction capacity similar to chlorine content (Ketcham et al., 1999).

In order to obtain zircon and apatites crystals needed for dating, whole rock samples were mechanically crushed and sieved and heavy minerals were recovered using conventional heavy liquid and magnetic methods at the Laboratorio de Separación de Minerales at the Departamento de Geología, Universidad de Chile.

U-Pb zircon dating was carried out by Apatite to Zircon Inc. using the single collector Finnigan Element II inductively coupled plasma–mass spectrometry (ICP-MS) of the Geoanalytical Laboratory at Washington State University, following the procedure described in Chang et al. (2006), Gehrels et al. (2008), and Shen et al. (2012). Sample preparation involved mounting in epoxy, polishing, and cleaning with approximately 5.5 M HNO<sub>3</sub> for 20 s at 21 °C. Zircon grains were then examined using nonpolarized, polychromatic, transmitted light and reflected light. A three-dimensional inspection using high magnification (1562.5X or 2000X), polychromatic light, and optical microscopy was made for both inclusions and zones of variable refractive index. Primary standard is Duluth Complex, and secondary standards are Fish Canyon Tuff, Mount Dromedary, and Temora. Between 48 and 21 grains were analyzed for each sample (Supporting Information 1). All reported ages and weighted mean ages have uncertainties at the two-sigma level (Supporting Information 1).

The AFT data were obtained at Apatite to Zircon Inc. using the laser ablation method described in Donelick et al. (2005) and Chew and Donelick (2012). Sample preparation for AFT analysis involved mounting of apatite grains in epoxy, polishing, and etching in 5.5 N HNO<sub>3</sub> for 20.0 s at 21 °C to reveal spontaneous fission tracks. Spontaneous fission tracks were counted in unpolarized light at 2000X magnification and laser ablation (LA)-ICP-MS analysis to determine <sup>238</sup>U was subsequently done in the same grain areas where spontaneous tracks were counted. In order to increase the number of tracks available for length measurement, apatite grains were irradiated with <sup>252</sup>Cf (Donelick & Miller, 1991) and etched a second time following the protocol described above. The track lengths and the angle between the track and the *c* axis were then measured. Additionally, for each grain age and track length measurement a Dpar value was obtained (Supporting Information 2). LA-ICP-MS analysis for AFT age determinations were carried out using the single-collector Finnigan Element II ICP-MS of the Geoanalytical Laboratory at Washington State University, following the procedure described in Donelick et al. (2005) and Chew and Donelick (2012). The primary standard is Durango; the secondary standards are Fish Canyon Tuff and Tioga Ash. ICP-MS and laser operating conditions and data acquisition parameters are shown in Supporting Information\_2.

Microprobe analysis was carried on 19 samples with at least 30 analyses per sample in grains parallel to the *c* axis (Table 1 and Supporting Information 4) to determine chlorine content. Since chlorine content and Dpar value are positively correlated (Barbarand et al., 2003; Carlson et al., 1999), some compositional effect might be influencing the obtained AFT ages. Unfortunately, it was not possible to analyze the chlorine content exactly in the same grains where AFT measurements were performed, because those analyses were made later at the University Paul Sabatier in Géoscience Environnement Toulouse Lab, France. Chemical composition ([Cl] wt%) was measured using a CAMECA SX50 microprobe with SAMx automation (see Supporting Information 4 for more details on microprobe operating conditions).

AHe age determinations were made in the Caltech Noble Gas Laboratory following the procedure described by Farley and Stockli (2002). Individual apatite grains >100 μm were screened for U-rich inclusions under a binocular microscope in polarized light at 120X magnification. Euhedral to subhedral inclusion-free grains were then hand-picked and their dimensions (length and width) measured to calculate the F<sub>T</sub> factor, correct to the effect of α-particles that are eventually ejected out of the grain (Farley & Stockli, 2002). Single apatite grains were later placed in platinum foil tubes and heated in-vacuum with a laser to degas and measure <sup>4</sup>He by MS. After He analysis, apatite grains in the platinum tubes were removed from the vacuum chamber, dissolved in nitric acid and spiked for U-Th determinations. Samples were spiked with <sup>235</sup>U and <sup>230</sup>Th, and U and Th isotopes ratios were measured on a single-collector Finnigan Element double-focusing inductively-coupled plasma mass spectrometer (Farley & Stockli, 2002). The analytical techniques are the same as described in Mahéo et al. (2009).

## 5. Results

### 5.1. Rock Ages

Previous geochronological ages are very scarce in the sampled rock units, and it was necessary to increase the available data set for our study. Therefore, six new U-Pb zircon weighted mean ages were obtained for samples collected in both geographic segments of this study (Figure 3 and Table 1). The obtained weighted mean ages are 118.8 ± 0.8 Ma (LC02, *n* = 48), 75.8 ± 7.1 Ma (LC09, *n* = 24), 61.6 ± 0.7 Ma (LC11, *n* = 21), 46.5 ± 0.6 Ma (LC07, *n* = 24), 39.1 ± 0.9 Ma (LL02, *n* = 23), and 42.4 ± 0.8 Ma (LL08 *n* = 24; Figure 3, Table 1, and Supporting Information 1).

The new U-Pb ages obtained and the available geochronological data published in this region (Table 1 and Figure 3) constrain the crystallization age of plutonic units from which the samples have been collected for thermochronometric analysis. Sampled units in the Coastal Cordillera, north and south of 31.5°S, consist of Lower and Upper Cretaceous plutonic rocks. North of 31.5°S, sampled units in the Main Cordillera consist of Lower Permian gneissic rocks and Lower Permian, Mid-Permian, Middle Triassic, Upper Triassic, Lower Cretaceous, Upper Cretaceous to Paleocene and Eocene plutonic rocks, whereas samples collected in the Frontal Cordillera consist of Middle Triassic granitoid bodies. Finally, south of 31.5°S sampled units in the Main Cordillera consist of Eocene and Paleocene plutonic rocks.

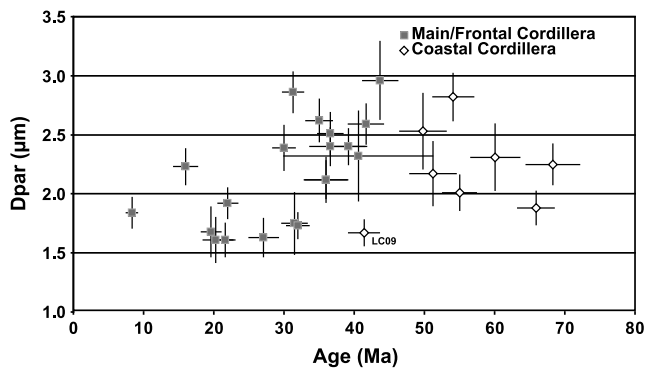


**Figure 5.** Dpar versus AFT ages of samples collected throughout the Coastal, Main and Frontal Cordilleras.

## 5.2. Thermochronology

In Tables 1, 28 new AFT pooled ages and 18 new AHe mean ages at  $\pm 1\sigma$  error are presented. Error in AHe mean ages is the  $\pm 1\sigma$  standard deviation on individual ages. Analytical uncertainties in AFT individual grain ages are related to U measurements and track counting uncertainty (see Supporting Information 2 for the number of grains analyzed for each sample), whereas in AHe individual grain ages the analytical error (Supporting Information 3) is related to uncertainties in U, Th, and He measurements and grain length uncertainty.

### 5.2.1. Coastal Cordillera

North of  $31.5^{\circ}\text{S}$ , AFT ages are  $65.9 \pm 2.7$  Ma,  $51.2 \pm 3.3$  Ma, and  $49.8 \pm 3.3$  Ma, decreasing from west to east (Figures 3 and 4a and Table 1), with Mean Track Length (MTL) ranging from  $14.22 \pm 1.55$  to  $13.57 \pm 2.11$   $\mu\text{m}$ . Dpar values are generally high, between  $2.53 \pm 0.32$  and  $1.88 \pm 0.14$   $\mu\text{m}$  (Table 1), suggesting potential high-T-annealing apatites (Donelick et al., 2005).

South of  $31.5^{\circ}\text{S}$ , AFT ages fall in an age range of  $68.3 \pm 3.8$  to  $41.4 \pm 2.2$  Ma (Figure 3), similar to the range of AFT ages obtained for samples of the Coastal Cordillera in the northern segment (Figure 4a). MTL are from  $14.68 \pm 1.34$  to  $13.88 \pm 1.9$   $\mu\text{m}$  (Table 1). Samples collected in the vertical profile from rocks assigned to the Lower Cretaceous plutonic belt (LC01, LC02, LC03, and LC04) present AFT ages similar within error (Table 1 and Figure 4a). Dpar values from apatites are generally high, ranging between mostly  $2.82 \pm 0.2$  and  $2.01 \pm 0.15$   $\mu\text{m}$  (Table 1), indicating that they probably correspond to high-T-annealing apatites (Donelick et al., 2005). Only one low Dpar value of  $1.67 \pm 0.11$   $\mu\text{m}$  (LC09; Figure 5), most representative of a low-T-annealing apatite (Donelick et al., 2005), is observed among samples from the Coastal Cordillera in the segment south of  $31.5^{\circ}\text{S}$  (Table 1). It is important to point out that sample LC09 yielded the youngest AFT age from the Coastal Cordillera (Figure 5). With respect to AHe data, four AHe mean ages were obtained from the Lower Cretaceous plutonic rocks of the vertical section in the segment south of  $31.5^{\circ}\text{S}$  (Table 1 and Figure 3). The mean AHe ages are  $30.5 \pm 3.8$  Ma (LC01,  $n = 5$ ),  $31.5 \pm 1.6$  Ma (LC02,  $n = 4$ ),  $23.5 \pm 6.5$  Ma (LC03,  $n = 6$ ), and  $28.5 \pm 4.0$  Ma (LC04,  $n = 3$ ), corresponding to the same age within error (Figure 4b).

### 5.2.2. Main Cordillera

North of  $31.5^{\circ}\text{S}$ , AFT ages obtained in Upper Cretaceous to Paleocene and Eocene units next to the topographic front range between  $39.2 \pm 2.3$  and  $31.3 \pm 1.5$  Ma, with MTL between  $15.00 \pm 1.44$  and  $13.86 \pm 1.30$   $\mu\text{m}$  and Dpar values between  $2.86 \pm 0.17$  and  $1.73 \pm 0.11$   $\mu\text{m}$ , representative of both high-T and low-T-annealing apatites (Table 1 and Figure 3). Farther east, AFT ages obtained for samples JA07, JA05, and LE02 collected from the Paleozoic crystalline core of the Main Cordillera present similar ages within errors of  $20.3 \pm 1.2$  Ma,  $19.6 \pm 0.7$  Ma, and  $22.0 \pm 1.4$  Ma, respectively (Table 1 and Figure 3) with MTL of  $14.12 \pm 1.38$ ,  $14.10 \pm 1.7$ , and  $13.79 \pm 1.52$   $\mu\text{m}$  (Table 1). Dpar values of JA07, JA05, and LE02 are  $1.61 \pm 0.19$ ,  $1.92 \pm 0.13$ , and  $1.68 \pm 0.21$   $\mu\text{m}$ , respectively, which may imply that dated apatites from those samples were low-T-annealing apatites (Donelick et al., 2005). Still farther east, samples LE03, LE04, and LE06, collected along the eastern border of the Main Cordillera (Figures 3 and 4a), present AFT ages of  $36.0 \pm 3.1$ ,  $27.2 \pm 2.1$ , and  $36.0 \pm 1.5$  Ma, respectively, identical within error (Table 1 and Figures 3 and 4a). MTLs of this samples range between  $13.88 \pm 1.76$  and  $12.97 \pm 1.86$   $\mu\text{m}$  (Table 1). In general, samples with Dpar values  $< 2$   $\mu\text{m}$  gave the youngest AFT ages (LE04), whereas samples with Dpar values  $> 2$   $\mu\text{m}$  have the oldest AFT ages (LE03 and LE06; Table 1 and Figure 5). Along the same segment, AHe mean ages from the Upper Cretaceous to Paleocene and Eocene units next to the topographic front are  $16.0 \pm 2.1$  Ma (LL08,  $n = 4$ ),  $19.0 \pm 3.4$  Ma (LL06,  $n = 4$ ),  $21.4 \pm 2.5$  Ma (LL07,  $n = 3$ ),  $17.6 \pm 2.7$  Ma (LL02,  $n = 4$ ), and  $18.1 \pm 1.2$  Ma (LL01,  $n = 4$ ) from north to south (Table 1 and Figures 3 and 4b). Farther east, AHe mean ages of sample LE02 collected along the Paleozoic crystalline core of the Main Cordillera and sample LE03 collected on the eastern border of the Main Cordillera are similar within errors at  $12.0 \pm 5.4$  ( $n = 4$ ) Ma and  $10.0 \pm 1.2$  Ma ( $n = 4$ ), respectively (Figure 3).

South of  $31.5^{\circ}\text{S}$ , AFT ages of samples collected next to the topographic front from the vertical profile on Eocene rocks are generally the same within error, ranging between  $41.7 \pm 2.5$  and  $30.0 \pm 1.6$  Ma, except for sample LC16 that has a much younger age of  $21.6 \pm 1.4$  Ma (Table 1 and Figure 3). MTL are between

$14.96 \pm 1.39$  and  $14.5 \pm 1.9$   $\mu\text{m}$ , whereas Dpar values are generally between  $2.62 \pm 0.18$  and  $2.32 \pm 0.38$   $\mu\text{m}$  and are representative of high-T-annealing apatites (Donelick et al., 2005; Table 1). The only exception corresponds to LC16, the youngest AFT age in the vertical section, which presents a Dpar value of  $1.61 \pm 0.14$   $\mu\text{m}$  (Table 1) representative of low-T-annealing apatites (Donelick et al., 2005). Farther south, the two AFT ages obtained from Upper Cretaceous to Paleocene plutonic belt are  $43.7 \pm 2.5$  (LC15) and  $16.0 \pm 1.7$  Ma (LC11) from west to east (Figures 3 and 4a), with MTL of  $14.59 \pm 2.17$  and  $14.57 \pm 1.5$   $\mu\text{m}$ , respectively, and Dpar values representative of high-T-annealing apatites (Donelick et al., 2005). In turn, AHe mean ages (Table 1 and Figures 3 and 4b) of samples collected from the vertical section of Eocene rocks are  $16.0 \pm 3.2$  Ma (LC05,  $n = 6$ ),  $15.5 \pm 0.9$  Ma (LC07,  $n = 3$ ),  $11.8 \pm 0.8$  Ma (LC08,  $n = 4$ ),  $17.4 \pm 3.9$  Ma (LC16,  $n = 3$ ),  $10.0 \pm 1.4$  Ma (LC17,  $n = 3$ ), and  $12.5 \pm 4.5$  Ma (LC18,  $n = 4$ ). Finally, toward the south samples from the Upper Cretaceous to Paleocene units display AHe mean ages of  $10.5 \pm 2.2$  Ma (LC15,  $n = 4$ ), and  $5.6 \pm 2.8$  Ma (LC15,  $n = 4$ ), getting younger toward the east (Figure 4b).

### 5.2.3. Frontal Cordillera

The easternmost sample collected north of  $31.5^\circ\text{S}$  is LE05 (Figures 3 and 4a) and presents the youngest AFT age of  $8.4 \pm 0.8$  Ma in this segment (Table 1 and Figure 4a) with MTL of  $14.10 \pm 1.48$   $\mu\text{m}$  (Table 1). The Dpar value of  $1.84 \pm 0.4$   $\mu\text{m}$  of sample LE05 is maybe representative of low-T-annealing apatites (Donelick et al., 2005). The AHe mean age obtained for sample LE05 ( $n = 4$ ) is  $6.9 \pm 0.6$  Ma, the youngest recognized north of  $31.5^\circ\text{S}$  (Figures 3 and 4b).

### 5.3. Apatite Chlorine Composition

Most of the apatites presenting high Dpar values are chlorine-rich ( $> 1\%$  within error), reaching chlorine contents as high as 2.3 wt% (LC02; Table 1). From the information given in section 5.2., it seems probable that Dpar values could indicate variable annealing kinetics controlling AFT ages. In fact, samples from the Main and Frontal Cordilleras with Dpar  $< 2$   $\mu\text{m}$  tend to present younger AFT ages than samples with Dpar  $> 2$   $\mu\text{m}$  (Table 1). Figure 5 shows that a positive correlation between Dpar values and AFT age exists in samples from the Coastal, Main, and Frontal Cordilleras. Most of the apatites presenting high Dpar values are chlorine-rich ( $> 1\%$  within error), reaching chlorine contents as high as 2.3 wt% (LC02; Table 1). Closure temperatures corresponding to the measured chlorine contents were calculated using HeFTy (Ketcham, 2005) assuming a typical cooling rate of  $10^\circ\text{C}/\text{Ma}$  (e.g., Djimbi et al., 2015). The closure temperatures estimated are as high as  $137^\circ\text{C}$  (LC02; Table 1), much higher than the nominal closure temperature of  $\sim 100^\circ\text{C}$  usually considered for the AFT system (Ketcham et al., 1999; Reiners & Brandon, 2006). When comparing the closure temperatures predicted by the chlorine content with those estimated by the Dpar values in the same sample, differences as high as  $18^\circ\text{C}$  are observed on some samples (LC02; Table 1), while others show no notable differences (e.g., LC15; Table 1). Regardless, the trends corroborate the positive correlation between Dpar and AFT ages, supporting the idea that composition-linked differences in thermal sensitivity are influencing the ages. As will be explained later, the divergences in predicted closure temperature for the AFT system between the Dpar and wt%Cl kinetic parameters may be critical when attempting to explain AFT and AHe data simultaneously.

## 6. Modeling of Thermochronological Data

We present next the procedure followed to analyze the thermochronological data and discuss the reliability of Dpar data measured in chlorine-rich apatites. We used the HeFTy program of Ketcham (2005) for thermal history modeling of our thermochronological data. AHe mean dates were used for the thermal history simulations. The annealing model of Ketcham et al. (1999) is used for AFT data and the Radiation Damage Accumulation Model (RDAAM) model of Flowers et al. (2009) for AHe data. The use of the RDAAM needs an additional explanation. This model uses a fission track annealing model to follow radiation damage accumulation due to the ejection of alpha particles inside the apatite crystal in the AHe system (Flowers et al., 2009). Radiation damage has an effect in the AHe system that is analogous to the chlorine effect in the AFT system, as higher amounts of radiation damage are associated with higher helium closure temperatures (Shuster et al., 2006). The effective U concentration (eU; Supporting Information 3) is the proxy used to account for radiation damage accumulation, provided that the apatite grains experienced the same thermal history (Flowers et al., 2009). The radiation damage effect manifests itself as a positive relationship between apatite AHe date and eU for slowly cooled samples or uniform dates regardless of eU for fast cooled samples (Flowers et al., 2009). As a calibration point, Durango apatite displays an eU  $\sim 50$  ppm, this raised its closure

temperature by about 15 °C according to RDAAM. While most of our samples display eU mean values lower than ~50 ppm, a few samples display higher eU mean values (Supporting Information 3), suggesting that helium closure temperature may be higher for those few samples due to radiation damage effect. For this reason, the RADAAM model was chosen for modeling AHe data.

For samples collected from the Lower Cretaceous plutonic belt in the Coastal Cordillera south of 31.5°S (LC01 to LC04) no possible thermal histories encompassing both AHe and AFT data are found using Dpar as the kinetic parameter. Although the Dpar values of these samples are higher than 2 μm (Table 1), they are not high enough to predict thermal histories that also encompass the associated AHe data, due to the large difference between AFT and AHe ages and the generally long tracks (>14 μm). Because the measured chlorine contents generally imply closure temperatures that are higher than the ones predicted by the Dpar values, use of Cl as a kinetic variable may be more appropriate here. However, because chlorine analyses were not performed exactly in the same grains on which fission tracks were counted and measured, an additionally layer of uncertainty is added to our thermochronological modeling. Despite this limitation, some models were run for sample LC02 using chlorine content as a kinetic parameter. Inversions that could simultaneously encompass both AHe and AFT data were obtained for LC02, corroborating that in this case, thermal modeling tend to be more successful by combining the AFT Cl data with AHe.

For the Main and Frontal Cordilleras, thermal models encompassing both, AFT and AHe data, are possible for samples with Dpar values <2 μm, which pass the chi-square test. This is in good agreement with the fact that apatites with Dpar <2 μm are considered fluorine-rich apatites, and no unusual compositional effects on AFT ages are to be expected (Ketcham et al., 1999). Therefore, herein thermal models are presented only for samples with Dpar values <2 μm that pass the Chi-square test.

For sample LL07 the initial constraint corresponds to the age of the rock (Table 1) at temperatures higher than 160–200 °C. The numbers of Dpar values measured on individual apatites grains from sample LL07 is 179. Most Dpar values are <2 μm (176) with only three measurements >2 μm. These three grains presenting Dpar values >2 μm were excluded from the modeling as no thermal modeling solutions were found when they were considered.

Sample JA07 presents an U-Pb age of ~284 Ma that is much older than its AFT age of ~20 Ma (Table 1). MTL >14 μm and Dpar <2 μm indicate that sample JA07 underwent accelerated cooling through the partial annealing zone (PAZ). The available geological information is insufficient to constrain the thermal history of this sample before it acquired its AFT age. Therefore, the initial constrain used is an age of approximately 25–30 Ma, older than its AFT age approximately 20 Ma, at temperatures higher than 160 °C.

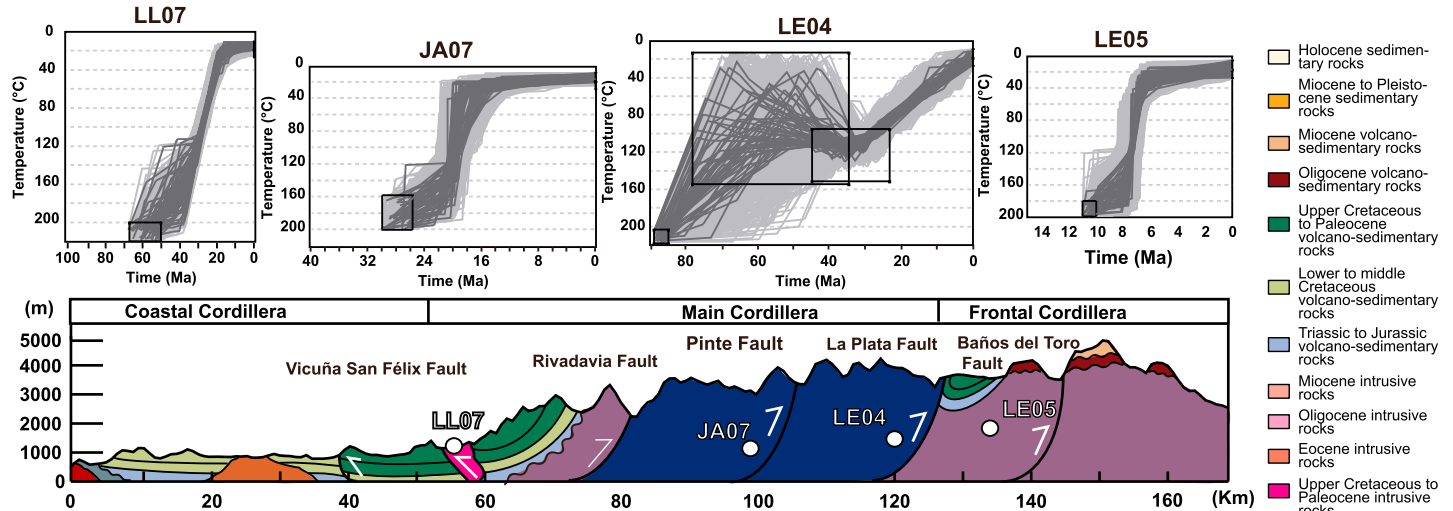
Despite its plutonic origin, LE04 presents two distinct populations of apatites with divergent AFT ages, Dpar, and track length values. This might be related to compositional differences between the individual apatite grains analyzed in this sample. Thermal models of LE04 were run as a two-population sample, as they pass the chi-square test. The age of the rock from which LE04 was sampled is approximately 285 Ma much older than its AFT age of approximately 27 Ma. According to the available geological information, the La Plata Fault (Figure 2) uplifted the block where LE04 was collected over Upper Jurassic rocks to the east, probably during the early to during the Peruvian (late Early to early Late Cretaceous) orogenic phase (e.g., Amilibia et al., 2008). Thus, we added additional constraints to explore the possibility of re-heating or quiescence during the Late Cretaceous to early Paleocene, with and initial constrain of 90–85 Ma at temperatures higher than 200 °C.

Sample LE05 was collected from Permo-Triassic rocks, presenting much younger AFT age of approximately 8 Ma and AHe age of approximately 7 Ma (Table 1). MTL >14 μm and Dpar <2 μm and similar AFT and AHe ages indicate that sample LE05 underwent accelerated cooling through PAZ and partial retention zone. The available geological information is not detailed enough to constrain the thermal history of this sample before it acquired its AFT age. Therefore, the initial constrain used is an age of 10–11 Ma, older than its AFT and AHe ages, at temperatures higher than 160 °C.

### 6.1. Coastal Cordillera

North of 31.5°S, no thermal models were run for sample G4 collected from the Lower Cretaceous plutonic belt Coastal Cordillera as no AHe ages were obtained for them. We made this to maintain a consistent basis for comparison with samples from the Coastal Cordillera south of 31.5°S, where thermal models include both AFT and AHe data. However, the AFT age of  $65.9 \pm 2.7$  Ma, with MTL >14 μm and Dpar <2 μm obtained in

a) North of 31.5° S



b) South of 31.5° S

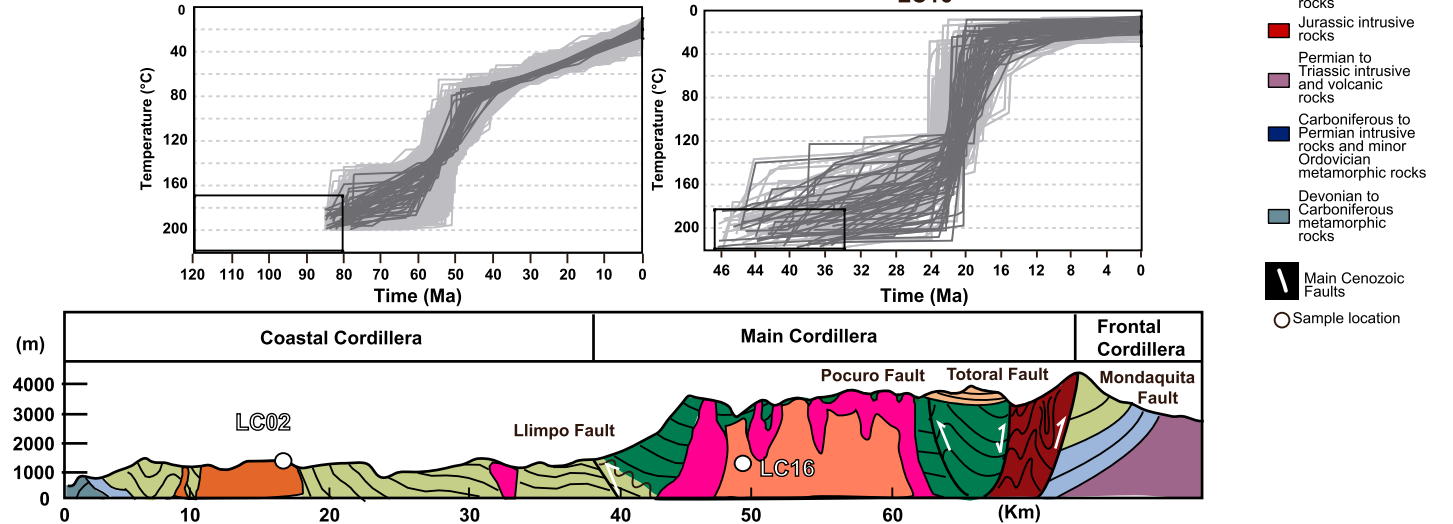


**Figure 6.** (a) Thermal history inversion models of thermochronological data obtained for samples LL07, JA07, LE04, and LE05 north of 31.5°S. The results are displayed as temperature-time (T-t) paths for good (black) and acceptable (gray) fit histories. Location of each sample is shown in a schematic geological cross section based in Mpodozis and Cornejo (1988), Nasi et al. (1990), and Pineda and Emparán (2006). (b) Thermal models of thermochronological data obtained for samples LL07, JA07, LE04, and LE05 north of 31.5°S. Location of each sample is shown in a schematic geological cross section based in Rivano and Sepúlveda (1991) and Jara and Charrier (2014). The results are displayed as temperature-time (T-t) paths for good (black) and acceptable (gray) fit histories.

sample G4 from the Lower Cretaceous plutonic belt, suggests that these rocks underwent rapid cooling though the PAZ during Late Cretaceous to Paleocene times.

South of 31.5°S, chlorine content was used as the AFT kinetic parameter for sample LC02 from the Lower Cretaceous plutonic belt (Figure 6b). The thermal models obtained suggest that rocks from the Lower Cretaceous plutonic belt in the Coastal Cordillera south of 31.5°S underwent accelerated cooling approximately 65–45 Ma and finally cooled gradually since approximately 45 Ma (Figure 6b). This result is similar to the thermal history deduced by AFT age, MTL, and Dpar values for sample G4 from the Lower Cretaceous plutonic belt north of 31.5°S.

**6.2. Main Cordillera**

North of 31.5°S, sample LL07 was collected from the domain next to the topographic front and belongs to the Upper Cretaceous to Paleocene intrusive belt (Pineda & Calderón, 2008). Thermal modeling of AFT and AHe

data from sample LL07 indicates that rocks from the Main Cordillera next to the topographic front in the segment north of 31.5°S were progressively cooled starting before approximately 40 Ma and extending until 20 Ma (Figure 6a). Farther east, thermal modeling of sample JA07 is consistent with a thermal history in which rocks from the Main Cordillera's crystalline core north of 31.5°S experienced accelerated cooling by approximately 22–14 Ma. Still farther east, sample LE04 was collected along the eastern border of the Main Cordillera in the same segment. Thermal models of LE04 are consistent with two periods of cooling (Figure 6a), including a first period of accelerated cooling starting at some moment during the Late Cretaceous or early Paleocene (approximately 90–55 Ma) and the second period of continuous cooling starting at some moment during the early Eocene to early Oligocene (approximately 40–30 Ma) and extending until the present day (Figure 6a).

South of 31.5°S, sample LC16 corresponds to an Eocene plutonic unit cropping out next to the topographic front. Thermal modeling of AFT and AHe data from sample LC16 is consistent with accelerated cooling from approximately 22 to 14 Ma throughout the Main Cordillera south of 31.5°S (Figure 6b).

### 6.3. Frontal Cordillera

Sample LE05 from the Frontal Cordillera corresponds to the easternmost sample collected in the segment north of 31.5°S (Figure 3). Thermal modeling of AFT and AHe data of sample LE05 shows one episode of accelerated cooling around approximately 7 Ma (Figure 6a).

## 7. Discussion

### 7.1. Magmatic Versus Tectonic Versus Climatic Effects

In the studied region, the several north-south oriented intrusive belts (with eastward decreasing ages) indicate almost continuous arc-related magmatic activity from the Early Jurassic to the middle Miocene (Figure 2). Therefore, in order to interpret thermochronological data in terms of exhumation, it is first necessary to exclude the possibility that the AFT and AHe ages would be reset by subsequent magmatism.

#### 7.1.1. Coastal Cordillera

North of 31.5°S, the AFT age measured on sample G4 (Figure 3 and Table 1) is the same within error as the available K-Ar and  $^{40}\text{Ar}$ - $^{39}\text{Ar}$  biotite and U-Pb zircon ages ranging between  $76 \pm 2$  and  $63.8 \pm 0.7$  Ma for the Upper Cretaceous to Paleocene belt (Arévalo et al., 2009). As previously explained AFT data of sample G4 suggest that these rocks underwent rapid cooling through the PAZ during the Upper Cretaceous to Paleocene. Although rocks belonging to the Upper Cretaceous to Paleocene belt do not intrude the Lower Cretaceous belt where the mentioned sample was collected, the subsurface geometry of Upper Cretaceous to Paleocene plutons, located approximately 30 km to the east, is unknown. Therefore, it is not possible to fully discard resetting due to subsequent magmatism as a probable explanation for the AFT ages. However, according to Arévalo et al. (2009) this area of the Coastal Cordillera underwent shortening near the Cretaceous-Paleocene boundary. Thus, AFT data on sample G4 possible reflect compressive events leading to the tectonic inversion of early Mesozoic extensional basins during the K-T (Cretaceous-Paleogene boundary) orogenic phase and syntectonic magmatism.

South of 31.5°S, sample LC09 from the southern Choapa Valley, which displays a U-Pb zircon age of  $75.8 \pm 7.1$  Ma (Figure 3 and Table 1), correlates with a series of Upper Cretaceous stocks, with K-Ar whole rock and biotite ages ranging between  $83 \pm 3$  and  $76 \pm 3$  Ma, that intrude the Lower Cretaceous plutonic belt mostly on its eastern border (Figure 3; Rivano & Sepúlveda, 1991; Emparán & Pineda, 2006). This age range overlaps with the episode of accelerated cooling shown by some of the thermal models with acceptable fitting for sample LC02 of the Lower Cretaceous plutonic belt (Figure 6b). However, these Upper Cretaceous stocks have been interpreted to be syntectonic with episodes of tectonic inversion affecting the early Mesozoic extensional basins from the Coastal Cordillera during the Peruvian or K-T phases (Emparán & Pineda, 2006). Therefore, thermochronological data across the Coastal Cordillera in this segment are probably reflecting the superimposed effects of both tectonic-related exhumation and syntectonic magmatism.

#### 7.1.2. Main Cordillera

North of 31.5°S, samples next to the topographic front were collected from granitoids belonging to the Upper Cretaceous to Paleocene and the Eocene plutonic belts (Figures 3 and 6a), with crystallization ages between approximately 69 and 67 Ma and approximately 55 and 34 Ma, respectively (Pineda & Emparán, 2006; Pineda

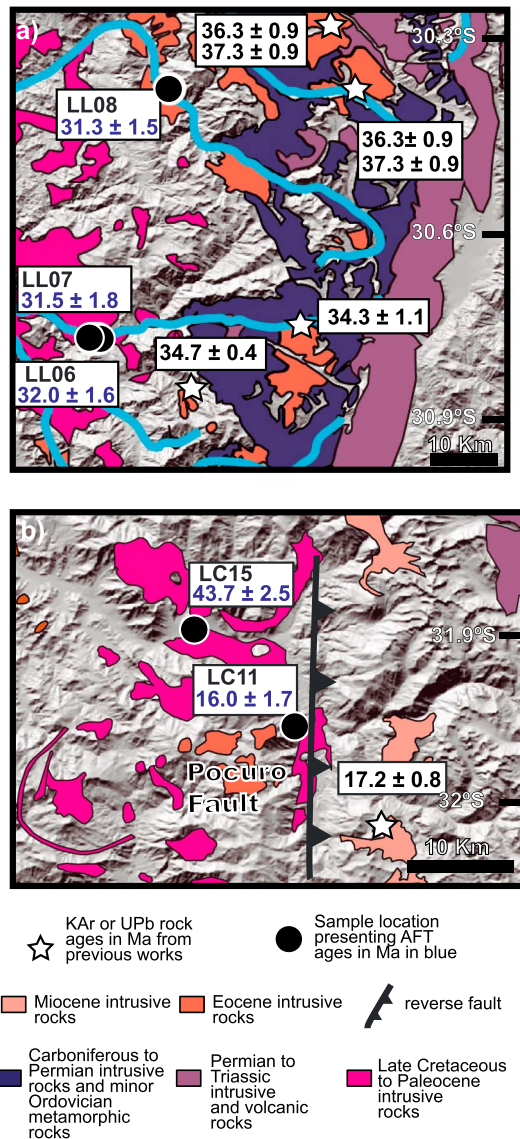


**Figure 7.** Locations in Figure 3. (a) The shaded relief image showing outcrops of plutonic units within the Limari valley with AFT ages (in blue) and K-Ar ages for Eocene and Oligocene plutonic units (in black) from Pineda and Calderón (2008). (b) The shaded relief image showing exposures of plutonic units within the southern Choapa Valley with AFT ages (in blue) and K-Ar ages for Miocene plutonic units (in black) from Rivano and Sepúlveda (1991).

& Calderón, 2008). Samples LL01 and LL02 present AFT ages of  $36.6 \pm 1.8$  and  $39.2 \pm 2.3$  Ma, respectively, that are identical within uncertainty as U-Pb ages of  $39.1 \pm 0.9$  Ma obtained in this work for LL02 (Table 1 and Figure 3). Thus, samples LL01 and LL02 were cooled through the PAZ of the AFT system almost simultaneously with their emplacement. In turn, samples LL06 and LL07 from Upper Cretaceous rocks and sample LL08 from the middle Eocene rocks yield late Eocene to early Oligocene AFT ages. These ages coincide fairly well with the emplacement ages of intrusive units exposed a few kilometers to the east (Pineda & Emparán, 2006; Pineda & Calderón, 2008; Figure 7a). Thus, AFT ages of LL06, LL07, and LL08 could reflect, at least in part, the effects of igneous cooling after the emplacement of late Eocene to early Oligocene plutonic rocks. On the contrary, AHe analyses of all samples collected next to the topographic front (LL01, LL02, LL06, LL07, and LL08) display ages between 21 and 16 Ma (Figure 8a), much younger than the AFT and U-Pb ages. Consistently, thermal modeling of the AFT and AHe data of sample LL07 indicates that these rocks were cooled progressively starting before approximately 40 and until 20 Ma (Figures 6a and 8a). Because magmatic cooling occurs in less than 1 Myr, the observed pattern of continuous and progressive cooling could not be reflecting such effect.

According to geochronological and structural data along the west-vergent Vicuña Fault (Figures 3 and 6a), shortening would have taken place during the mid-late Eocene between 45 and 35 Ma (Pineda & Emparán, 2006; Pineda & Calderón, 2008). Thus, AFT ages ranging between approximately 39 and 33 Ma next to the topographic front (Figure 8a) probably reflect both the effects of igneous cooling and exhumation related to contractional deformation along this fault and building of the Incaic Range north of  $31.5^\circ\text{S}$ , as previously interpreted for AFT data obtained along the Main Cordillera next to the topographic front in the Elqui Valley (Cembrano et al., 2003; Lossada et al., 2017). Progressive cooling until approximately 20 Ma ago is in good agreement with paleogeographic reconstructions pointing out that the Incaic Range was a main morphological feature long after the mid-late Eocene tectonic event (Bissig & Riquelme, 2010; Charrier et al., 2009; Riquelme et al., 2007). However, the main faults along the western topographic front in this segment have been sealed by intrusive units with ages between approximately 45 and 35 Ma (Pineda & Emparán, 2006; Pineda & Calderón, 2008). Thus, the endurance of the Incaic Range as the main locus of exhumation until the early Miocene may be in part related to the dry climate in this part of the Andes. It is possible that the drying associated with global rapid cooling of climate at the Eocene-Oligocene transition (e.g., Zachos et al., 2001; Dupont-Nivet et al., 2007) may have prevented the eastward advance of retrograde erosion toward the interior of the Main Cordillera.

Farther east along the segment north of  $31.5^\circ\text{S}$ , samples JA05, JA07, and LE02 were collected from the Paleozoic crystalline core of the Main Cordillera (Figures 3 and 6a). As no lower to middle Miocene plutonic rocks intrude this part of the Main Cordillera, the period of accelerated cooling through the PAZ around approximately 22–14 Ma recognized for sample JA07 (Figures 6a and 8a) is more probably related to exhumation. Southward from where JA07 was collected, but still in the segment north of  $31.5^\circ\text{S}$ , sample LE02 presents a Dpar  $< 2 \mu\text{m}$ . Similar to JA07, this sample presents an AFT age of approximately 22 Ma (Figure 3) and long fission tracks ( $> 14 \mu\text{m}$ ; Table 1) indicating that it cooled through the PAZ shortly after 22 Ma. Taking together the AFT age and the AHe age of  $12 \pm 5.4$  Ma for sample LE02 (Figure 3 and Table 1), they are consistent with rapid exhumation through both the PAZ and partial retention zone during the early to middle Miocene. Therefore, AFT and AHe data from this sample are consistent with the thermal modeling of AFT



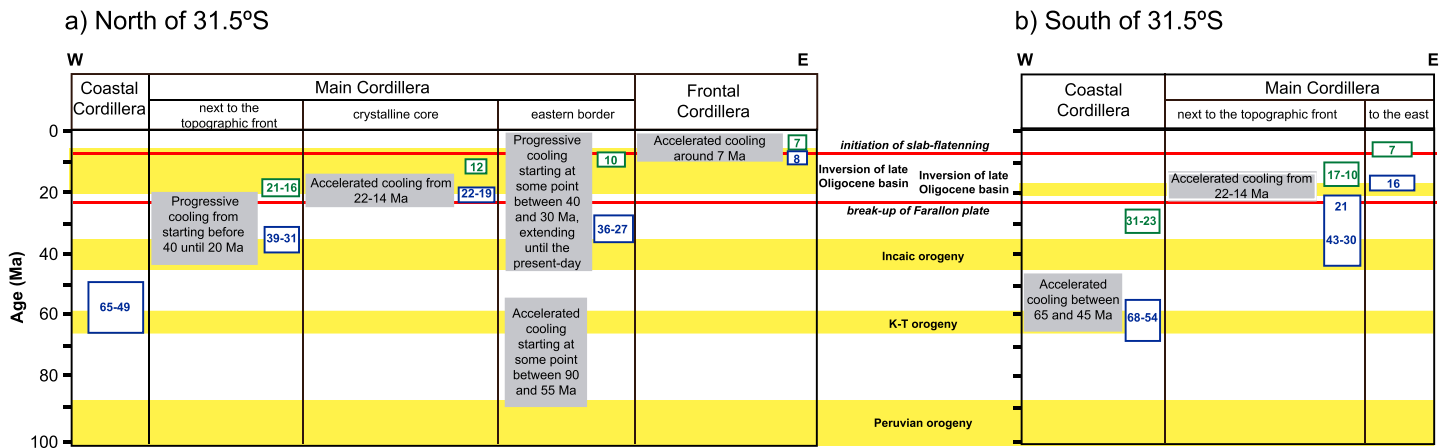


**Figure 8.** Summary of thermochronological data for segments (a) north of 31.5°S and (b) south of 31.5°S. AFT ages in blue, AHe ages in green, and thermal histories derived by modeling of thermochronometric data marked by grey squares. Tectonic events marked by pale yellow squares and large-scale plate tectonics events marked by red lines.

data of JA07. Finally, AFT and AHe data from samples JA07 and LE02 are interpreted as reflecting tectonic-induced exhumation during the early to middle Miocene along the Paleozoic core of the Main Cordillera in the segment north of 31.5°S. Although it is not clear which faults may be involved in this exhumation event at the latitude of the Elqui River, the east vergent Pinte Fault (Moscoco & Mpodozis, 1988) may be responsible for early to middle Miocene accelerated exhumation in the Huasco River area in the northern part of the studied region.

Still farther east along the segment north of 31.5°S, at the eastern border of the Main Cordillera, the first period of accelerated cooling during the Late Cretaceous or early Paleocene (ca. 90–55 Ma) recognized for sample LE04 (Figures 6a and 8a) cannot be related to magmatic effects as intrusive rocks of such age crop out farther west, at the border between the Coastal and Main Cordilleras (Figures 2, 3 and 6a). Accelerated cooling during the Late Cretaceous or early Paleocene is interpreted as rather reflecting exhumation of rocks related to partial tectonic inversion of early Mesozoic extensional basins during the Peruvian (late Early to early Late Cretaceous) or K-T (Cretaceous-Paleogene boundary) orogenic phases as it has been shown to have occurred along the border between the Main and Frontal Cordilleras in the Copiapó River area approximately 50 km north of the studied region (Martínez et al., 2012). The following period of cooling observed in this sample that started at some point during the Eocene or early Oligocene (approximately 40–30 Ma) is not easily explicable (Figures 6a and 8a). During the Oligocene, an extensional intra-arc basin developed in the Frontal Cordillera, represented by the outcrops of Doña Ana Hill (Figures 2 and 6a). However, extensional conditions started approximately 27 Ma ago (Winocur et al., 2015), strictly after the beginning of the second period of cooling identified in sample LE04. Thus, cooling starting between approximately 40–30 Ma may not be related to exhumation induced by the extensional conditions leading to development of the intra-arc basin to the east.

Recently published geological maps (Salazar & Coloma, 2016) and morphostructural analysis (Rossel et al., 2016) recognize Eocene contraction taking place at the border between the Main and Frontal Cordilleras along the Huasco River in the northern part of the studied region. Moreover, geochemical signatures of Eocene plutonic rocks emplaced in the Elqui River area (Bocatoma stocks, Winocur et al., 2015) indicate that these rocks developed in a compressional arc environment. Thus, the cooling onset at approximately 40–30 Ma for LE04 and AFT ages approximately 36–27 Ma for LE03 and LE06 (Figure 8a) are interpreted as reflecting exhumation of rocks due to late Eocene compression affecting the eastern border of the Main Cordillera north of 31.5°S. Reverse movements along the east vergent La Plata Fault (Figures 2 and 6a) may have uplifted the eastern border of the Main Cordillera during the late Eocene in the area where LE04 was collected. From the late Eocene onward, exhumation presents a progressive trend after this contractional event, similar to what has been described at the western border of the Main Cordillera (sample LL07) along the same segment (Figure 8a). There are no geological records for shortening taking place after the Oligocene along the eastern border of the Main Cordillera north of 31.5°S (Salazar & Coloma, 2016; Nasi et al., 1990). Thus, it

is interpreted that landscape in this area has been in a transient state since the Oligocene as a consequence of the semiarid to arid climatic conditions established after rapid cooling of climate at the Eocene-Oligocene transition (e.g., Zachos et al., 2001; Dupont-Nivet et al., 2007).

In the segment south of 31.5°S, sample LC16 collected next to the topographic front, is the only sample for which a coherent thermal history was obtained (Figure 6b). According to this model, the area next to the topographic front underwent an episode of accelerated cooling at ca. 22–14 Ma, which is in good agreement with AHe ages between ca. 17 and 10 Ma obtained for the rest of the samples collected next to the topographic front (Figure 8b). Exposures of Miocene plutonic rocks are mostly constrained to the area south of 32°S (Figure 2), and therefore Miocene magmatism could not have reset thermochronological ages. Thus, accelerated cooling at 22–14 Ma (Figure 8b) suggests that rocks next to the topographic front south of 31.5°S underwent a main period of tectonic-induced exhumation during the early to mid-Miocene. Tectonic movements along the west vergent Llimpo Fault could be responsible for uplifting the block where LC16 was collected (Figures 2 and 6b). No thermal models were obtained for the rest of the samples collected next to the topographic front due to the large difference between AFT and AHe ages, long fission tracks  $>14 \mu\text{m}$  and too-small Dpar values. However, the measured AFT ages approximately 43–30 Ma (Figure 8b) cannot be ruled out as they indicate that rocks from the Main Cordillera next to the topographic front south of 31.5°S were cooled through PAZ coevally or shortly after their emplacement given by U-Pb ages at approximately 46 Ma (Figure 3). Although no late Eocene reverse faults have been recognized south of 30°S, paleomagnetic reconstructions show that block rotations between 31.5 and 33°S mainly occurred in the early to mid-Miocene but after an initial Eocene-Oligocene phase (Arriagada et al., 2013). Thus, AFT ages approximately 43–30 Ma close to the topographic front south of 31.5°S are probably related to this earlier phase. Farther structural geology works are needed to better understand the Incaic Orogeny in this segment. One possibility is that the Llimpo Fault was active during the late Eocene shortening too. The easternmost sample collected south of 31.5°S, LC11, presents an AFT age of  $16 \pm 1.7$  Ma (Figure 8b), which is similar to the emplacement ages of early Miocene intrusive rocks cropping out a few kilometers to the east (Figure 7b). Here the southernmost extension of the Llimpo Fault is unclear (Figure 2). However, given that this fault has been interpreted to have uplifted the eastern block from approximately 22 to 14 Ma in the same segment, but farther north, one possible explanation is that the AFT age of  $16 \pm 1.7$  Ma could be reflecting both cooling after emplacement of the early Miocene belt and coeval exhumation due to west vergent tectonic movements along the Llimpo Fault. Conversely, the AHe age of  $6.9 \pm 0.4$  Ma for sample LC11 (Figure 8b) is much younger and cannot be related to any intrusions (Figure 7b). Thus, the easternmost sample collected south of 31.5°S, LC11, is interpreted to have been exhumed at approximately 7 Ma. It has been suggested that global acceleration of glacial erosion in mountain belts may occur related to the onset of glaciation in the poles (e.g., Herman et al., 2013). In particular, it is known that glaciation in Patagonia started approximately 7 Ma (Mercer & Sutter, 1982). However, sample LC11 was collected near the bottom of a fluvial valley presenting no signs of previous glacial erosion. Therefore, exhumation around 7 Ma cannot be related to enhance glacial erosion and thus was probably induced by tectonic-driven erosion, although it is unclear which fault may be responsible for exhumation.

### 7.1.3. Frontal Cordillera

Thermal models for sample LE05 point to a main period of accelerated cooling affecting the Frontal Cordillera at about approximately 7 Ma (Figures 6a and 8a). As no intrusive units presenting a similar age are recognized for this area (Bissig et al., 2011), magmatic reheating is ruled out. As explained for the easternmost sample collected in the segment south of 31.5°S, sample LE05 was collected near the bottom of a fluvial valley presenting no signs of previous glacial erosion. On the contrary, accelerated cooling around 7 Ma indicates that exhumation is coeval with the final stages of inversion of the late Oligocene intra-arc basin (Winocur, 2010) and uplift of planation surfaces near the international border with Argentina (Bissig et al., 2002). Tectonic movements along the east vergent Baños del Toro Fault may be responsible for exhumation approximately 7 Ma along the Frontal Cordillera in the Elqui valley where LE05 was collected.

## 7.2. North to South Variability in Exhumation Timing

Thermochronological data from north-central Chile show that exhumation in this Andean region shifted gradually to the east in Late Cretaceous to late Neogene times. However, the obtained data indicate latitudinal

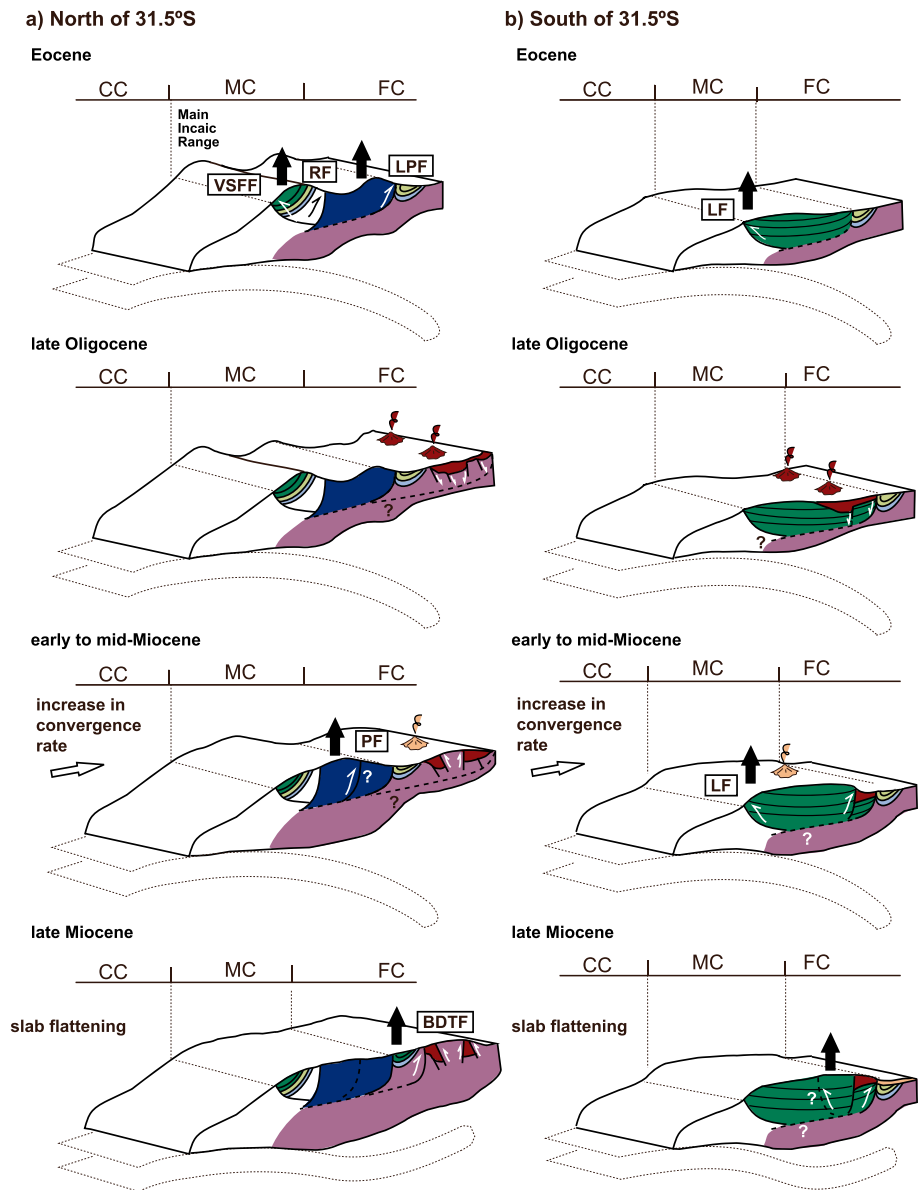


**Figure 9.** Schematic chronologic evolution of the Andes of north-central Chile and the development of the western topographic front since the Eocene in the segments (a) north of 31.5°S and (b) south of 31.5°S. Geological legend in Figure 2. The black arrows mark areas that underwent uplift-induced exhumation throughout the Cenozoic interpreted from thermochronological data. CC = Coastal Cordillera, MC = Main Cordillera, FC = Frontal Cordillera. VSFF = Vicuña-San Félix Fault, RF = Rivadavia Fault, LPP = La Plata Fault, PF = Pinte Fault, BDTF = Baños del Toro Fault, LF = Llimpo Fault.

variations in the main periods of exhumation related to the development of the western topographic front north and south of 31.5°S (Figures 8 and 9).

For the segment between 28.5° and 31.5°S, AFT data indicate tectonic-induced exhumation related to the development of the western topographic front began before approximately 40 Ma (Figure 8a), building the Incaic Range (Charrier et al., 2007; 2009; Lossada et al., 2017; Martínez et al., 2017) along the western border of the Main Cordillera (Figure 9a). AFT ages of approximately 36–27 Ma (Figure 8a) and the period of exhumation starting at some point between approximately 40 and 30 Ma (Figure 8a) identified by thermal modeling indicate that exhumation also took place on the eastern border of the Main Cordillera during the late Eocene (Figure 9a). Besides the Coastal Cordillera, the western and eastern borders of the Main Cordillera are the domains where the inherited architecture from the early Mesozoic extensional period is

mostly preserved (Figures 2, 6a, and 9a). The reverse Vicuña-San Félix and Rivadavia Faults along the western border of the Main Cordillera and the La Plata Fault along the eastern border of the Main Cordillera (Figure 6a) correspond to early Mesozoic rift faults, inverted in the late Eocene according to the data presented here (Figure 9a). This is in good agreement with previous work showing that Eocene shortening in the Chilean Andes is mainly controlled by preexisting early Mesozoic extensional faults (Amilibia et al., 2008; Martínez et al., 2017). In this scenario, the Paleozoic crystalline core of the Main Cordillera (Figure 6a) seems to have acted as a buttress during Eocene inversion, allowing shortening to occur only at the western and eastern borders of the Main Cordillera where the inverted early Mesozoic rift-faults are located (Figure 9a). Thermal models indicate that landscapes along the western and eastern border of the Main Cordillera have been in a transient state until the present-day (Figure 9a). This may be in part due to prevailing semiarid to arid climatic conditions after global cooling at the Eocene-Oligocene transition in north-central Chile. Such pattern of exhumation is consistent with the low millennial denudation rate (Carretier et al., 2013; Aguilar et al., 2014) and the large proportion of low relief surfaces preserved in catchments of this region (Fariás et al., 2008; Rehak et al., 2010; Aguilar et al., 2013; Rodríguez et al., 2015). Thermochronological models and interpretation of AFT and AHe data indicate that exhumation was resumed by the early to middle Miocene affecting the crystalline core of the Main Cordillera at approximately 22–14 Ma (Figure 8a), coevally with the early stages of tectonic inversion of the late Oligocene intra-arc basin developed along the Frontal Cordillera to the east (Figure 9a). Finally, modeling of AFT and AHe data indicates that the locus of exhumation shifted eastward into the Frontal Cordillera approximately 7 Ma ago (Figure 8a) coevally with the late stages of tectonic inversion of the late Oligocene intra-arc basin (Figure 9a, Winocur, 2010).

For the segment between 31.5° and 32°S, thermal modeling of AFT and AHe shows a main period of accelerated exhumation and shortening at approximately 22–14 Ma next to the western topographic front in the Main Cordillera (Figure 8b), coevally with the tectonic inversion of the late Oligocene intra-arc basin developed to the east (Figure 9b). Prior to this main period of shortening in the early to middle Miocene, AFT ages approximately 43–30 Ma (Figure 8b) suggest that an initial period of exhumation occurred in the late Eocene (Figure 8b). The absence of the Paleozoic crystalline core of the Main Cordillera (Figure 6b), which apparently acted as a buttress during late Eocene shortening, may have prevented major shortening and uplift from occurring south of 31.5°S (Figure 9b). Finally, AHe data of the easternmost sample collected south of 31.5°S (Figure 8b) indicate that the locus of exhumation across the Main Cordillera moved to the east at approximately 7 Ma (Figure 9b).

### 7.3. Large-Scale Tectonic Controls on Uplift-Induced Exhumation

Some authors have interpreted that the main periods of exhumation and shortening in north-central Chile are a consequence of the arrival to the studied region of the southward propagating subduction of the Juan Fernandez ridge (Arriagada et al., 2013; Cembrano et al., 2003). The ridge reached the northern limit of studied region at 28°S around 12 Ma ago and the southern limit at 32°S around 10 Ma ago (Yáñez et al., 2001). The AFT and AHe data presented here indicate that the main periods of exhumation throughout the studied region occurred around approximately 22–14 Ma and approximately 7 Ma. Thus, exhumation seems unrelated to the southward migration of the Juan Fernandez ridge. This is understandable considering that the onset of flat subduction is what actually drives a highly compressive tectonic regime in the continental margin, not the passing of the Juan Fernandez ridge (Pardo et al., 2002). Martinod et al. (2010) explained that the delay between the arrival of the ridge and the onset of flat subduction may be due to an insufficient volume of the ridge subducted at that time to make the slab buoyant or to the rapid southward migration of the ridge before 10 Ma that precluded development of a horizontal slab. These authors also emphasize that the most accepted evidence of the onset of flat subduction comes from the evolution of arc volcanism. Thus, the initiation of slab flattening in the studied region occurred at some point between 9 Ma, when andesitic magmatism in the main arc ended, and 5 Ma, after which arc volcanism became restricted to the Sierras Pampeanas (Kay & Gordillo, 1994). Regionally, early to middle Miocene accelerated exhumation between 22 and 14 Ma north and south of 31.5°S better correlates with a main period of late Oligocene to mid-Miocene increased deformation recognized throughout the entire Central Andes from the Altiplano-Puna plateau (e.g., Charrier et al., 2012; Jordan et al., 2010) to the Main Cordillera of central Chile at 32–36°S (Charrier et al., 2002; Fariás et al., 2010). This episode of increased deformation is thought to be caused by the dramatic increase in convergence rate between the oceanic and continental plates occurring after

breakup of the Farallon into the Nazca and Cocos Plates ca. 23 Ma (Pardo-Casas & Molnar, 1987; Seton et al., 2012; Somoza, 1998). In turn, late Miocene accelerated exhumation around 7 Ma in the Frontal Cordillera north of 31.5°S and in the eastern reaches of the Main Cordillera south of 31.5°S may be related with the onset of flat subduction and the concomitant shift of deformation toward the east as recognized by Fosdick et al. (2015) for the Frontal Cordillera in Argentina at 30°S. Thus, the absence of late Miocene to Pliocene exhumation ages next to the topographic front in the studied region seems to better correlates with the concomitant shift of deformation toward the east, than with present-day precipitation gradients along the strike of the Andes.

It is also important to discuss how the data set presented here fits the proposed tectonic models for the studied region. Two main morphotectonic models have been proposed for the area of central Chile to the south, which differ in the interpretation for the main vergence assigned to the first-order structure controlling morphotectonic evolution. Farías et al. (2008, 2010) proposes a crustal-scale décollement underneath the Andean orogen as the first-order structure and an associated second-order westward fault, the San Ramón Fault, controlling forearc uplift. On the other hand, Armijo et al. (2010) recognizes westward fault propagation and related folding along the San Ramón Fault (also named WAT, West Andean Thrust), which steps down eastward, constituting the first-order structure. Armijo et al. (2010) argued for a post 25 Ma activity of the WAT along the western topographic front at the latitude of Santiago, 200 km south from the studied region, extrapolating their results for the entire Central Andes. However, the thermochronological ages and modeling presented here show that no significant exhumation younger than mid-Miocene occurred along the western topographic front in the studied region. Thus, the WAT, possibly corresponding to the west-vergent Vicuña-San Felix and Llimpo faults, has not played a significant role since the mid-Miocene in north-central Chile between 28.5 and 32°S.

## 8. Conclusions

Large differences among AFT and AHe ages and thermal modeling of thermochronological data indicate that little exhumation in the Coastal Cordillera took place during most of the Cenozoic, probably after tectonic deformation during the Late Cretaceous or early Paleocene.

The Main Cordillera show latitudinal differences in exhumation patterns north and south of 31.5°S. North of 31.5°S, Cenozoic exhumation began before approximately 40–30 Ma at the western and eastern limits of the Main Cordillera, building the Incaic Range, that was progressively exhumed in a transient state until the early Miocene. Later, accelerated exhumation focused on the core of the Main Cordillera and in the Frontal Cordillera at approximately 22–14 Ma and approximately 7 Ma, respectively. South of 31.5°S, accelerated exhumation in the Main Cordillera mainly occurred around ~ 22–14 Ma next to the topographic front, whereas to the east exhumation occurred until the late Miocene.

Latitudinal differences in exhumation timing north and south of 31.5°S could be explained by the absence of the Paleozoic crystalline core of the Main Cordillera south of 31.5°S, which seems to have acted as a buttress during late Eocene shortening, preventing major shortening and exhumation to occur southwards from 31.5°S.

The early to middle Miocene episode of accelerated exhumation recognized north and south of 31.5°S is probably a consequence of a considerable increase in convergence rate between the oceanic and continental plates occurring after the Farallon breakup into the Nazca and Cocos Plates at 23 Ma.

Finally, late Miocene exhumation along the Frontal Cordillera north of 31.5°S and the eastern reaches of the Main Cordillera south of 31.5°S is probably the consequence of the onset of flat subduction throughout the studied region.

## References

- Aguilar, G., Carretier, S., Regard, V., Vassallo, R., Riquelme, R., & Martinod, J. (2014). Grain size-dependent  $^{10}\text{Be}$  concentrations in alluvial stream sediment of the Huasco Valley, a semi-arid Andes region. *Quaternary Geochronology*, *19*, 163–172. <https://doi.org/10.1016/j.quageo.2013.01.011>
- Aguilar, G., Riquelme, R., Martinod, J., & Darrozes, J. (2013). Role of climate and tectonics in the geomorphologic evolution of the semiarid Chilean Andes between 27–32°S. *Andean Geology*, *40*(1), 79–101. <https://doi.org/10.5027/andgeoV40n1-a04>

### Acknowledgments

This study was supported in part by the Chilean Government through the Comisión Nacional de Ciencia y Tecnología (CONICYT) (Anillo ACT-18 project, AMTC), the Advanced Mining Technology Center (AMTC) of the Facultad de Ciencias Físicas y Matemáticas-Universidad de Chile, FONDECYT (Fondo Nacional de Desarrollo Científico y Tecnológico) projects 11085022, 1120272, and 1161806, and ECOSud-Conicyt program (project C11U02). Additional support was obtained from IRD Project “Erosión en los Andes.” This study is part of the PhD thesis of M. P. Rodríguez, which was supported by a four-year grant from CONICYT. We deeply thank Ken Farley for opening his laboratory to M. P. Rodríguez to perform AHe analysis and Lindsey Hedges for helping with AHe sample preparation. We thank Ray Donelick for acquiring in his lab the AFT data. We also thank David Shuster for valuable discussions on AHe data interpretation during an invited visit to the study region. The manuscript was greatly improved by comments by David Barbeau and an anonymous reviewer. U-Pb analysis, AFT, and AHe single grain data and apatite composition are available from the supporting information.

- Alvarado, P., Beck, S., Zandt, G., Araujo, M., & Triep, E. (2005). Crustal deformation in the south-central Andes backarc terranes as viewed from regional broad-band seismic waveform modelling. *Geophysical Journal International*, *163*(2), 580–598. <https://doi.org/10.1111/j.1365-246X.2005.02759.x>
- Alvarado, P., & Ramos, V. A. (2011). Earthquake deformation in the northwestern Sierras Pampeanas of Argentina based on seismic waveform modelling. *Journal of Geodynamics*, *51*(4), 205–218. <https://doi.org/10.1016/j.jog.2010.08.002>
- Álvarez, J., Mpodozis, C., Arriagada, C., Astini, R., Morata, D., Salazar, E., et al. (2011). Detrital zircons from late Paleozoic accretionary complexes in north-central Chile (28°–32°S): Possible fingerprints of the Chilena terrane. *Journal of South American Earth Sciences*, *32*(4), 460–476. <https://doi.org/10.1016/j.jsames.2011.06.002>. Retrieved from <Go to ISI>://WOS:000298464900016
- Amilibia, A., Sàbat, F., Mcclay, K. R., Muñoz, J. A., Roca, E., & Chong, G. (2008). The role of inherited tectono-sedimentary architecture in the development of the central Andean mountain belt: Insights from the Cordillera de Domeyko. *Journal of Structural Geology*, *30*, 1520–1539. <https://doi.org/10.1016/j.jsg.2008.08.005>
- Arévalo, C., Mourgues, F., & Chávez, F. R. (2009). Geología del Área Vallenar-Domeyko, Región de Atacama, scale 1:100.000, Serv. Nac. de Geol. y Miner, Santiago.
- Armijo, R., Lacassin, R., Coudurier-Curveur, A., & Carrizo, D. (2015). Coupled tectonic evolution of Andean orogeny and global climate. *Earth Science Review*, *143*, 1–35. <https://doi.org/10.1016/j.earscirev.2015.01.005>
- Armijo, R., Rauld, R., Thiele, R., Vargas, G., Campos, J., Lacassin, R., & Kausel, E. (2010). The West Andean Thrust, the San Ramon Fault, and the seismic hazard for Santiago, Chile. *Tectonics*, *29*, TC2007. <https://doi.org/10.1029/2008TC002427>. Retrieved from <Go to ISI>://000276029200001
- Arriagada, C., Ferrando, R., Córdova, L., Morata, D., & Roperch, P. (2013). The Maipo Orocline: A first scale structural feature in the Miocene to Recent geodynamic evolution in the central Chilean Andes. *Andean Geology*, *40*(3). <https://doi.org/10.5027/andgeoV40n3-a02>
- Barbarand, J., Carter, A., Wood, I., & Hurford, T. (2003). Compositional and structural control of fission-track annealing in apatite. *American Mineralogist*, *198*(1–2), 107–137. [https://doi.org/10.1016/S0009-2541\(02\)00424-2](https://doi.org/10.1016/S0009-2541(02)00424-2)
- Barnes, J. B., & Ehlers, T. A. (2009). End member models for Andean Plateau uplift. *Earth-Science Reviews*, *97*(1–4), 105–132. <https://doi.org/10.1016/j.earscirev.2009.08>
- Barnes, J. B., Ehlers, T. A., McQuarrie, N., Sullivan, P. B. O., & Pelletier, J. D. (2006). Eocene to recent variations in erosion across the Central Andean fold-thrust belt, northern Bolivia: Implications for plateau evolution. *Earth and Planetary Science Letters*, *248*(1–2), 118–133. <https://doi.org/10.1016/j.epsl.2006.05.018>
- Bissig, T., Clark, A. H., Lee, J. K. W., & Hodgson, C. J. (2002). Miocene landscape evolution and geomorphologic controls on epithermal processes in the El Indio-Pascua Au-Ag-Cu belt, Chile and Argentina. *Economic Geology*, *97*(5), 971–996. <https://doi.org/10.2113/97.5.971>. [online] Retrieved from: <Go to ISI>://WOS:000178050500003
- Bissig, T., Lee, J. K. W., Clark, A. H., & Heather, K. B. (2011). The Cenozoic History of Volcanism and Hydrothermal Alteration in the Central Andean Flat-Slab Region: New 40 Ar–39 Ar Constraints from the El Indio–Pascua Au (–Ag, Cu) Belt, 29°20′–30°30′ S. *International Geology Review*, *43*(4), 312–340. <https://doi.org/10.1080/00206810109465016>. Retrieved from Accessed 30 August 2012 <http://www.tandfonline.com/doi/abs/10.1080/00206810109465016>
- Bissig, T., & Riquelme, R. (2010). Andean uplift and climate evolution in the southern Atacama Desert deduced from geomorphology and supergene alunite-group minerals. *Earth and Planetary Science Letters*, *299*(3–4), 447–457. <https://doi.org/10.1016/j.epsl.2010.09.028>. Retrieved from <http://www.sciencedirect.com/science/article/B6V61-518F0CS-3/2/bb88a23fa1f480e57b22ff13837997b7>
- Cahill, T., & Isacks, B. L. (1992). Seismicity and Shape of the Subducted Nazca Plate. *Journal of Geophysical Research*, *97*(B12), 17,503–17,529. Retrieved from <Go to ISI>://A1992JY18900019.
- Carretier, S., Regard, V., Vassallo, R., Aguilar, G., Martinod, J., Riquelme, R., et al. (2013). Slope and climate variability control of erosion in the Andes of central Chile. *Geology*, *41*(2), 195–198. <https://doi.org/10.1130/G33735.1>
- Carlson, W. D. (1990). Mechanisms and kinetics of apatite fission-track annealing. *American Mineralogist*, *75*, 1120–1139.
- Carlson, W. D., Donelick, R. A., & Ketcham, R. A. (1999). Variability of apatite fission-track annealing kinetics: I. Experimental results. *American Mineralogist*, *84*(9), 1213–1223. Retrieved from <Go to ISI>://WOS:000082349700001
- Cembrano, J., Zentilli, M., Grist, A., & Yáñez, G. (2003). Nuevas edades de trazas de fisión para Chile Central (30–34°S): Implicancias en el alzamiento y exhumación en los Andes desde el Cretácico, paper presented at X Congr. Geol. Chileno, Universidad de Concepción, Concepción, Chile.
- Chang, Z., Vervoort, J. D., McClelland, W. C., & Knaack, C. (2006). U-Pb dating of zircon by LA-ICP-MS. *Geochemistry, Geophysics, Geosystems*, *7*, Q05009. <https://doi.org/10.1029/2005GC001100>
- Charrier, R., Baeza, O., Elgueta, S., Flynn, J. J., Gans, P., Kay, S. M., et al. (2002). Evidence for Cenozoic extensional basin development and tectonic inversion south of the flat-slab segment, southern Central Andes, Chile (33°–36°S). *Journal of South American Earth Sciences*, *15*(1), 117–139. [https://doi.org/10.1016/S0895-9811\(02\)00009-3](https://doi.org/10.1016/S0895-9811(02)00009-3). Retrieved from <Go to ISI>://WOS:000175725400009
- Charrier, R., Farías, M., & Maksiav, V. (2009). Evolución tectónica, paleogeográfica y metalogénica durante el Cenozoico en los Andes de Chile norte y central e implicaciones para las regiones adyacentes de Bolivia y Argentina. *Revista de la Asociación Geológica Argentina*, *65*, 5–35.
- Charrier, R., Hérial, G., Pinto, L., García, M., Riquelme, R., Farías, M., & Muñoz, N. (2012). Cenozoic tectonic evolution in the Central Andes in northern Chile and west central Bolivia: Implications for paleogeographic, magmatic and mountain building evolution. *International Journal of Earth Sciences*, *102*(1), 235–264. <https://doi.org/10.1007/s00531-012-0801-4>, <http://www.springerlink.com/index/10.1007/s00531-012-0801-4>
- Charrier, R., Pinto, L., & Rodríguez, M. P. (2007). Tectonostratigraphic evolution of the Andean Orogen in Chile. In T. Moreno & W. Gibbons (Eds.), *The geology of Chile* (pp. 21–114). London: The Geological Society. <https://doi.org/10.1144/GOCH.3>
- Chew, D. M., & Donelick, R. A. (2012). Combined apatite fission track and U-Pb dating by LA-ICP-MS and its application in apatite provenance analysis. *Mineralogical Association of Canada Short Course*, *42*, (May), 219–147.
- Costa, C. H., Audemard, F. A., Bezerra, F. H. R., Lavenue, A., Machette, M. N., & Paris, G. (2006). An overview of the main Quaternary deformation of South America. *Earth Surface Processes*, *61*(4), 461–479.
- Crowley, K. D. (1993). Mechanisms and kinetics of apatite fission-track annealing discussion. *American Mineralogist*, *78*, 210–212.
- Crowley, K. d., Cameron, M., & Schaefer, R. I. (1991). Experimental studies of annealing of etched fission tracks in fluorapatite. *Geochimica et Cosmochimica Acta*, *55*(5), 1449–1465. [https://doi.org/10.1016/0016-7037\(91\)90320-5](https://doi.org/10.1016/0016-7037(91)90320-5)
- Dewey, J. F., & Bird, J. M. (1970). Mountain belts and the new global tectonics. *Journal of Geophysical Research*, *75*(14), 2625–2647. <https://doi.org/10.1029/JB075i014p02625>
- Djimbi, M. D., Gautheron, C., Roques, J., Tassan-Got, L., Gerin, C., & Simoni, E. (2015). Impact of apatite chemical composition on (U-Th)/He thermochronometry: An atomistic point of view. *Geochimica et Cosmochimica Acta*, *167*, 162–176. <https://doi.org/10.1016/j.gca.2015.06.017>

- Donelick, R., & Miller, D. S. (1991). Enhanced TINT fission track densities in low spontaneous track density apatites using 252Cf-derived fission fragment tracks. A model and experimental observations. *Nuclear Tracks and Radiation Measurements*, 18(3), 301–307. [https://doi.org/10.1016/1359-0189\(91\)90022-A](https://doi.org/10.1016/1359-0189(91)90022-A)
- Donelick, R. A. (1993). A method of fission track analysis utilizing bulk chemical etching of apatite, Patent 5267274, *U.S. Patent and Trademark Off., Washington, D. C.*
- Donelick, R. A., O'Sullivan, P. B., & Ketcham, R. A. (2005). Apatite fission-track analysis. *Reviews in Mineralogy and Geochemistry*, 58(1), 49–94. <https://doi.org/10.2138/rmg.2005.58.3>. Retrieved from Accessed 22 July 2012 <http://rmg.geoscienceworld.org/cgi/doi/10.2138/rmg.2005.58.3>
- Dupont-Nivet, G., Krijgsman, W., Langereis, C. G., Abels, H. A., Dai, S., & Fang, X. (2007). Tibetan plateau aridification linked to global cooling at the Eocene-Oligocene transition. *Nature*, 445(7128), 635–638. <https://doi.org/10.1038/nature05516>
- Emparan, C., & Pineda, G. (2006). Geología del Area Andacollo-Puerto Aldea, Región de Coquimbo, scale 1:100.000, Serv. Nac. de Geol. y Miner, Santiago.
- Fariás, M. (2007). Tectónica y erosión en la evolución del relieve de los Andes de Chile central durante el Neógeno. Universidad de Chile. Retrieved from [http://www.tesis.uchile.cl/tesis/uchile/2007/farias\\_mt/sources/farias\\_mt.pdf](http://www.tesis.uchile.cl/tesis/uchile/2007/farias_mt/sources/farias_mt.pdf)
- Fariás, M., Charrier, R., Carretier, S., Martinod, J., Fock, A., Campbell, D., et al. (2008). Late Miocene high and rapid surface uplift and its erosional response in the Andes of central Chile (33°–35°S). *Tectonics*, 27, TC1005. <https://doi.org/10.1029/2006TC002046>
- Fariás, M., Charrier, R., Comte, D., Martinod, J., & Hérail, G. (2005). Late Cenozoic deformation and uplift of the western flank of the Altiplano: Evidence from the depositional, tectonic, and geomorphologic evolution and shallow seismic activity (northern Chile at 19°30'S). *Tectonics*, 24, TC4001. <https://doi.org/10.1029/2004TC001667>. Retrieved from <Go to ISI>://WOS:000230484000001
- Fariás, M., Comte, D., Charrier, R., Martinod, J., David, C., Tassarà, A., et al. (2010). Crustal-scale structural architecture in central Chile based on seismicity and surface geology: Implications for Andean mountain building. *Tectonics*, 29, TC3006. <https://doi.org/10.1029/2009TC002480>
- Farley, K. A., & Stockli, D. F. (2002). (U-Th)/He dating of phosphates: Apatite, monazite, and xenotime. *Reviews in Mineralogy and Geochemistry*, 48(1), 559–577. <https://doi.org/10.2138/rmg.2002.48.15>. Retrieved from Accessed 30 August 2012 <http://rmg.geoscienceworld.org/cgi/doi/10.2138/rmg.2002.48.15>
- Flowers, R. M., Ketcham, R. A., Shuster, D. L., & Farley, K. A. (2009). Apatite (U – Th)/He thermochronometry using a radiation damage accumulation and annealing model. *Geochimica et Cosmochimica Acta*, 73(8), 2347–2365. <https://doi.org/10.1016/j.gca.2009.01.015>
- Fosdick, J. C., Carrapa, B., & Ortiz, G. (2015). Faulting and erosion in the Argentine Precordillera during changes in subduction regime: Reconciling bedrock cooling and detrital records. *Earth and Planetary Science Letters*, 432, 73–83.
- Gallagher, K., Brown, R., & Johnson, C. (1998). Fission track analysis and its applications to geological problems. *Annual Reviews of Earth Plane Sciences*, 26(1), 519–572. <https://doi.org/10.1146/annurev.earth.26.1.519>
- García, M., & Hérail, G. (2005). Fault-related folding, drainage network evolution and valley incision during the Neogene in the Andean Precordillera of Northern Chile. *Geomorphology*, 65(3–4), 279–300. Retrieved from <Go to ISI>://000227347600007
- Gautheron, C., Tassan-Got, L., Barbarand, J., & Pagel, M. (2009). Effect of alpha-damage annealing on apatite (U-Th)/He thermochronology. *Chemical Geology*, 266(3–4), 157–170. <https://doi.org/10.1016/j.chemgeo.2009.06.001>
- Gehrels, G. E., Valencia, V. A., & Ruiz, J. (2008). Enhanced precision, accuracy, efficiency, and spatial resolution of U-Pb ages by laser ablation-multicollector-inductively coupled plasma-mass spectrometry. *Geochemistry, Geophysics, Geosystems*, 9, Q03017. <https://doi.org/10.1029/2007GC001805>
- Gleadow, A. J. W., Kohn, B. P., Brown, R. W., O'Sullivan, P. B., & Raza, A. (2002). Fission track thermotectonic imaging of the Australian continent. *Tectonophysics*, 349(1–4), 5–21. [https://doi.org/10.1016/S0040-1951\(02\)00043-4](https://doi.org/10.1016/S0040-1951(02)00043-4)
- Green, P. F., Duddy, I. R., Gleadow, A. J. W., Tingate, P. R., & Laslett, G. M. (1986). Thermal annealing of fission tracks in apatite 1. A qualitative description. *Chemical Geology*, 59(4), 237–253. [https://doi.org/10.1016/0009-2541\(86\)90048-3](https://doi.org/10.1016/0009-2541(86)90048-3)
- Hall, S. R., Farber, D. L., Audin, L., & Finkel, R. C. (2012). Recently active contractile deformation in the forearc of southern Peru. *Earth and Planetary Science Letters*, 337–338, 85–92. <https://doi.org/10.1016/j.epsl.2012.04.007>
- Herman, F., Seward, D., Valla, P. G., Carter, A., Kohn, B., Willett, S. D., & Ehlers, T. A. (2013). Worldwide acceleration of mountain erosion under a cooling climate. *Nature*, 504(7480), 423–426. <https://doi.org/10.1038/nature12877>
- Jara, P., & Charrier, R. (2014). Nuevos antecedentes geocronológicos y estratigráficos en la Cordillera Principal de Chile central entre 32° y 32°30'S Implicancias paleogeográficas y estructurales. *Andean Geology*, 41(1). <https://doi.org/10.5027/andgeoV41n1-a07>
- Jordan, T. E., Isacks, B. L., Allmendinger, R. W., Brewer, J. A., Ramos, V. A., & Ando, C. J. (1983). Andean tectonics related to geometry of subducted Nazca Plate. *Geological Society of America Bulletin*, 94(3), 341–361. [https://doi.org/10.1130/0016-7606\(1983\)94<341:atrtgo>2.0.co;2](https://doi.org/10.1130/0016-7606(1983)94<341:atrtgo>2.0.co;2). Retrieved from <Go to ISI>://WOS:A1983QN40400003
- Jordan, T. E., Nester, P. L., Blanco, N., Hoke, G. D., Dávila, F., & Tomlinson, A. J. (2010). Uplift of the Altiplano-Puna plateau: A view from the west. *Tectonics*, 29, TC5007. <https://doi.org/10.1029/2010TC002661>
- Kay, S. M., & Gordillo, C. E. (1994). Pocho Volcanic-Rocks and the Melting of Depleted Continental Lithosphere Above a Shallowly Dipping Subduction Zone in the Central Andes. *Contributions to Mineralogy and Petrology*, 117(1), 25–44. <https://doi.org/10.1007/bf00307727>
- Kay, S. M., & Mpodozis, C. (2002). Magmatism as a probe to the Neogene shallowing of the Nazca plate beneath the modern Chilean flat-slab. *Journal of South American Earth Sciences*, 15(1), 39–57. [Pii s0895-9811\(02\)00005-6](https://doi.org/10.1016/S0895-9811(02)00005-6). Retrieved from <Go to ISI>://WOS:000175725400005
- Ketcham, R. A. (2005). Forward and inverse modeling of low-temperature thermochronometry data. *Reviews in Mineralogy and Geochemistry*, 58(1), 275–314. <https://doi.org/10.2138/rmg.2005.58.11>
- Ketcham, R. A., Donelick, R. A., & Carlson, W. D. (1999). Variability of apatite fission-track annealing kinetics: III. Extrapolation to geological time scales. *American Mineralogist*, 84, 1235–1255. <https://doi.org/10.2138/Am.2006.464>
- Lamb, S. (2000). Active deformation in the Bolivian Andes, South America. *Journal of Geophysical Research*, 105(B11), 25,627–25,653. <https://doi.org/10.1029/2000JB900187>
- Litvak, V. D., Poma, S., Kay, S. M., & Valle, E. (2007). Paleogene and Neogene magmatism in the Valle del Cura region: New perspective on the evolution of the Pampean flat slab, San Juan province, Argentina. *Journal of South American Earth Sciences*, 24(2–4), 117–137. <https://doi.org/10.1016/j.jsames.2007.04.002>
- Lossada, A. C., Giambiagi, L., Hoke, G. D., Fitzgerald, P. G., Creixell, C., Murillo, I., et al. (2017). Thermochronologic evidence for Late Eocene Andean mountain building at 30°S. *Tectonics*, 36, 2693–2713. <https://doi.org/10.1002/2017TC004674>
- Mahéo, G., Saleeby, J., Saleeby, Z., & Farley, K. A. (2009). Tectonic control on southern Sierra Nevada topography, California. *Tectonics*, 28, TC6006. <https://doi.org/10.1029/2008TC002340>
- Maksaeu, V., Munizaga, F., Zentilli, M., & Charrier, R. (2009). Fission track thermochronology of Neogene plutons in the Principal Andean Cordillera of central Chile (33–35°S): Implications for tectonic evolution and porphyry Cu-Mo mineralization. *Andean Geology*, 36(2), 153–171.

- Maksaev, V., & Zentilli, M. (1999). Fission track thermochronology of the Domeyko Cordillera, northern Chile; implications for Andean tectonics and porphyry copper metallogenesis. *Exploration and Mining Geology, Special Issue on Latin American Mineral Deposits*, 8, 65–89.
- Martin, M. W., Clavero, J., & Mpodozis, C. (1999). Late Paleozoic to Early Jurassic tectonic development of the high. *Journal of South American Earth Sciences*, 12(1), 33–49. [https://doi.org/10.1016/S0895-9811\(99\)00003-6](https://doi.org/10.1016/S0895-9811(99)00003-6)
- Martínez, F., Arriagada, C., Mpodozis, C., & Peña, M. (2012). The Lautaro Basin: A record of inversion tectonics in northern Chile. *Journal of South American Earth Sciences*, 39(2).
- Martínez, F., Arriagada, C., Peña, M., Deckart, K., & Charrier, R. (2016). Tectonic styles and crustal shortening of the Central Andes “Pampean” flat-slab segment in northern Chile (27–29°S). *Tectonophysics*, 667(23), 144–162. <https://doi.org/10.1016/j.tecto.2015.11.019>
- Martínez, F., Parra, M., Arriagada, C., Mora, A., Bascañan, S., & Peña, M. (2017). Late Cretaceous to Cenozoic deformation and exhumation of the Chilean Frontal Cordillera (28°–29°S), Central Andes. *Journal of Geodynamics*, 111(April), 31–42. <https://doi.org/10.1016/j.jog.2017.08.004>
- Martinod, J., Husson, L., Roperch, P., Guillaume, B., & Espurt, N. (2010). Horizontal subduction zones, convergence velocity and the building of the Andes. *Earth and Planetary Science Letters*, 299(3–4), 299–309. <https://doi.org/10.1016/j.epsl.2010.09.010>
- Mercer, J. H., & Sutter, J. F. (1982). Late miocene-earliest pliocene glaciation in southern Argentina: Implications for global ice-sheet history. *Palaeogeography, Palaeoclimatology, Palaeoecology*, 38(3–4), 185–206. [https://doi.org/10.1016/0031-0182\(82\)90003-7](https://doi.org/10.1016/0031-0182(82)90003-7)
- Moscoso, R., & Mpodozis, C. (1988). Estilos estructurales en el Norte Chico de Chile (28–31°S), Regiones de Atacama y Coquimbo. *Revista Geologica de Chile*, 15(2), 151–166.
- Mpodozis, C., Brockway, H., Marquardt, C., & Perelló, J. (2009). Geocronología U/Pb y tectónica de la región de Los Pelambres-Cerro Mercedario: implicancias para la evolución cenozoica de Los Andes del centro de Chile y Argentina, paper presented at XII Congr. Geol. Chileno, Universidad de Chile, Santiago, Chile.
- Mpodozis, C., & Cornejo, P. (1988). Hoja Pisco Elqui, IV Región de Coquimbo, scale 1:50.000, Serv. Nac. de Geol. y Miner, Santiago.
- Muñoz, N., & Charrier, R. (1996). Uplift of the western border of the Altiplano on a west-vergent thrust system, Northern Chile. *Journal of South American Earth Sciences*, 9(3–4), 171–181. Retrieved from <Go to ISI>://A1996VU24500003.
- Nasi, C., Moscoso, R., & Maksaev, V. (1990). Hoja Guanta, Regiones de Atacama y Coquimbo, scale 1:50.000, Serv. Nac. de Geol. y Miner, Santiago.
- Ortiz, G., Alvarado, P., Fosdick, J., Perucca, L., Saez, M., & Venerdini, A. (2015). Active deformation in the northern Sierra de Valle Fertil, Sierras Pampeanas, Argentina. *Journal of South American Earth Sciences*, 64, 339–350. <https://doi.org/10.1016/j.jsames.2015.08.015>
- Pankhurst, R. J., Millar, I., & Hervé, F. (1996). A Permo-Carboniferous U-Pb age for part of the Guanta Unit of the Elqui-Limari Batholith at Rio del Transito, Northern Chile. *Revista Geologica de Chile*, 23, 35–42.
- Pardo, M., Comte, D., & Monfret, T. (2002). Seismotectonic and stress distribution in the central Chile subduction zone. *Journal of South American Earth Sciences*, 15(1), 11–22. [https://doi.org/10.1016/S0895-9811\(02\)00003-2](https://doi.org/10.1016/S0895-9811(02)00003-2). Retrieved from <Go to ISI>://WOS:000175725400003
- Pardo-Casas, F., & Molnar, P. (1987). Relative motion of the Nazca (Farallon) and South American plates since late Cretaceous time. *Tectonics*, 6(3), 233–248. <https://doi.org/10.1029/TC006i003p00233>
- Pérez, A., Ruiz, J. A., Vargas, G., Rauld, R., Rebolledo, S., & Campos, J. (2013). Improving seismotectonics and seismic hazard assessment along the San Ramón fault at the eastern border of Santiago City, Chile. *Natural Hazards*, 71(1), 243–274. <https://doi.org/10.1007/s11069-013-0908-3>
- Pineda, G., & Calderón, M. (2008). Geología del área Monte Patria-El Maqui, Región de Coquimbo. Servicio Nacional de Geología y Minería, scale 1:100.000, Serv. Nac. de Geol. y Miner, Santiago.
- Pineda, G., & Emparán, C. (2006). Geología del área Vicuña-Pichasca, Región de Coquimbo. Servicio Nacional de Geología y Minería, scale 1:100.000, Serv. Nac. de Geol. y Miner, Santiago.
- Pinto, L., Herail, G., Fontan, F., & de Parseval, P. (2007). Neogene erosion and uplift of the western edge of the Andean Plateau as determined by detrital heavy mineral analysis. *Sedimentary Geology*, 195(3–4), 217–237. <https://doi.org/10.1016/j.sedgeo.2006.08.001>
- Ramos, V. A., Cristallini, E. O., & Perez, D. J. (2002). The Pampean flat-slab of the Central Andes. *Journal of South American Earth Sciences*, 15(1), 59–78. [https://doi.org/10.1016/S0895-9811\(02\)00006-8](https://doi.org/10.1016/S0895-9811(02)00006-8)
- Rauld, R. A. (2011). Deformación cortical y peligro sísmico asociado a la falla San Ramón en el Frente Cordillerano de Santiago, Chile central (33°S). Tesis para optar al grado de Doctor en Ciencias, Mención Geología, 443 pp., Dep. de Geol., Univ. de Chile, Santiago.
- Rehak, K., Niedermann, S., Preusser, F., Strecker, M. R., & Echter, H. P. (2010). Late Pleistocene landscape evolution in south-central Chile constrained by luminescence and stable cosmogenic nuclide dating. *Geological Society of America Bulletin*, 122(7–8), 1235–1247. <https://doi.org/10.1130/B26545.1>
- Reiners, P. W., & Brandon, M. T. (2006). Using Thermochronology To Understand Orogenic Erosion. *Annual Review of Earth and Planetary Sciences*, 34(1), 419–466. <https://doi.org/10.1146/annurev.earth.34.031405.125202>
- Riquelme, R., Hérial, G., Martinod, J., Charrier, R., & Darrozes, J. (2007). Late Cenozoic geomorphologic signal of Andean forearc deformation and tilting associated with the uplift and climate changes of the Southern Atacama Desert (26°S–28°S). *Geomorphology*, 86(3–4), 283–306. doi:<https://doi.org/10.1016/j.geomorph.2006.09.004>. Retrieved from Accessed 28 January 2012 <http://linkinghub.elsevier.com/retrieve/pii/S0169555X06004089>
- Rivano, S., & Sepúlveda, P. (1991). Hoja Illapel, Región de Coquimbo, scale 1:50.000, Serv. Nac. de Geol. y Miner, Santiago.
- Rodríguez, M. P., Aguilar, G., Urresty, C., & Charrier, R. (2015). Neogene landscape evolution in the Andes of north-central Chile between 28.5 and 32°S: Interplay between tectonic and erosional processes. In S. A. Sepúlveda, et al. (Eds.), *Geodynamic processes in the Andes of central Chile and Argentina*, Geological Society, London, *Special Publications* (Vol. 399, pp. 419–446). <https://doi.org/10.1144/SP399.15>
- Rossel, K., Aguilar, G., Salazar, E., Martinod, J., Carretier, S., Pinto, L., & Cabré, A. (2016). Chronology of Chilean Frontal Cordillera building from geochronological, stratigraphic and geomorphological data insights from Miocene intramontane-basin deposits. *Basin Research*, 30, 289–310. <https://doi.org/10.1111/br.12221>
- Salazar, E., & Coloma, F. (2016). Geología del área Cerros de Cantaritos-Laguna Chica, Región de Atacama. Servicio Nacional de Geología y Minería, scale 1:100.000, Serv. Nac. de Geol. y Miner, Santiago.
- Sanchez, C., Bricchau, S., Riquelme, R., Carretier, S., Bissig, T., Lopez, C., et al. (2017). Exhumation history and timing of supergene copper mineralisation in an arid climate: New thermochronological data from the Centinela District, Atacama, Chile. *Terra Nova*, 30(1), 78–85. <https://doi.org/10.1111/ter.12311>
- Sernageomin (2003). Carta Geológica de Chile, scale 1:1.000.000, Serv. Nac. de Geol. y Miner, Santiago.
- Seton, M., Müller, R. D., Zahirovic, S., Gaina, C., Torsvik, T., Shephard, G., & Chandler, M. (2012). Global continental and ocean basin reconstructions since 200 Ma. *Earth Science Review*. <https://doi.org/10.1016/j.earscirev.2012.03.002>
- Shen, C. B., Donelick, R. A., O’Sullivan, P. B., Jonckheere, R., Yang, Z., She, Z. B., et al. (2012). Provenance and hinterland exhumation from LA-ICP-MS zircon U-Pb and fission-track double dating of Cretaceous sediments in the Jiangnan Basin, Yangtze block, central China. *Sedimentary Geology*, 281, 194–207. <https://doi.org/10.1016/j.sedgeo.2012.09.009>



- Somoza, R. (1998). Updated Nazca (Farallon) - South America relative motions during the last 40 My: Implications for mountain building in the Central Andean region. *Journal of South American Earth Sciences*, 11(3), 211–215. Retrieved from <go to ISI>://000078067600001.
- Shuster, D. L., Flowers, R. M., & Farley, K. A. (2006). The influence of natural radiation damage on helium diffusion kinetics in apatite. *Earth and Planetary Science Letters*, 249(3–4), 148–161. <https://doi.org/10.1016/j.epsl.2006.07.028>
- Stalder, N., Herman, F., Reiners, P. W., & Aguilar, G. (2017). Late Cenozoic acceleration of erosion in the Southern Central Andes revealed by low temperature thermochronology. In *EGU General Assembly*.
- Tassara, A. (2005). Interaction between the Nazca and South American plates and formation of the Altiplano-Puna plateau: Review of a flexural analysis along the Andean margin (15 degrees-34 degrees S). *Tectonophysics*, 399(1–4), 39–57. <https://doi.org/10.1016/j.tecto.2004.12.014>
- Vargas, G., Klinger, Y., Rockwell, T. K., Forman, S. L., Rebolledo, S., Baize, S., et al. (2014). Probing large intraplate earthquakes at the west flank of the Andes. *Geology*, 42(12), 1083–1086. <https://doi.org/10.1130/G35741.1>
- Victor, P., Oncken, O., & Glodny, J. (2004). Uplift of the western Altiplano plateau: Evidence from the Precordillera between 20° and 21°S (northern Chile). *Tectonics*, 23, TC4004. <https://doi.org/10.1029/2003TC001519>. Retrieved from <Go to ISI>://WOS:000222919100001
- Winocur, D (2010). Geología y estructura del Valle del Cura y el sector central del Norte Chico, provincia de San Juan y IV Región de Coquimbo, Argentina y Chile, (PhD thesis). University de Bs. Aires, Buenos Aires, Argentina.
- Winocur, D. A., Litvak, V. D., & Ramos, V. A. (2015). Magmatic and tectonic evolution of the Oligocene Valle del Cura Basin, Main Andes of Argentina and Chile: Evidence for generalized extension. In *Geodynamic processes in the Andes of central Chile and Argentina* (Vol. 399, pp. 109–130). London: Geological Society.
- Yáñez, G., Ranero, C. R., Von Huene, R., & Díaz, J. (2001). Magnetic anomaly interpretation across the southern Central Andes (32°–34°S): The role of the Juan Fernández Ridge in the late Tertiary evolution of the margin. *Journal of Geophysical Research*, 106(B4), 6325–6345. <https://doi.org/10.1029/2000JB900337>
- Zachos, J., Pagani, M., Sloan, L., Thomas, E., & Billups, K. (2001). Trends, Rhythms, and Aberrations in Global Climate 65 Ma to Present. *Science*, 292(April), 686–693.